

Effect of core–mantle and tidal torques on Mercury’s spin axis orientation  
Stanton J. Peale<sup>a</sup>, Jean-Luc Margot<sup>b,c</sup>, Steven A. Hauck, II<sup>d</sup>, Sean C. Solomon<sup>e,f</sup>

<sup>a</sup>Department of Physics, University of California, Santa Barbara, CA 93106.

<sup>b</sup>Department of Earth, Planetary, and Space Sciences, University of California, Los Angeles CA 90095.

<sup>c</sup>Department of Physics and Astronomy, University of California, Los Angeles, CA 90095.

<sup>d</sup>Department of Earth, Environmental, and Planetary Sciences, Case Western Reserve University, Cleveland, OH 44106.

<sup>e</sup>Department of Terrestrial Magnetism, Carnegie Institution of Washington, Washington, DC 20015.

<sup>f</sup>Lamont-Doherty Earth Observatory, Columbia University, Palisades, NY 10964.

### Abstract

The rotational evolution of Mercury’s mantle plus crust and its core under conservative and dissipative torques is important for understanding the planet’s spin state. Dissipation results from tidal torques and viscous, magnetic, and topographic torques contributed by interactions between the liquid core and solid mantle. For a spherically symmetric core–mantle boundary (CMB), the system goes to an equilibrium state wherein the spin axes of the mantle and core are fixed in the frame precessing with the orbit, and in which the mantle and core are differentially rotating. This equilibrium exhibits a mantle spin axis that is offset from the Cassini state by larger amounts for weaker core–mantle coupling for all three dissipative core–mantle coupling mechanisms, and the spin axis of the core is separated farther from that of the mantle, leading to larger differential rotation. Relatively strong core–mantle coupling is necessary to bring the mantle spin axis to a position within the uncertainty in its observed position, which is close to the Cassini state defined for a completely solid Mercury. Strong core–mantle coupling means that Mercury’s response is closer to that of a solid planet. Measured or inferred values of parameters in all three core–mantle coupling mechanisms for a spherically symmetric CMB appear not to accomplish this requirement. For a hydrostatic ellipsoidal CMB, pressure coupling dominates the dissipative effects on the mantle and core positions, and dissipation with pressure coupling brings the mantle spin solidly to the Cassini state. The core spin goes to a position displaced from that of the mantle by about 3.55 arcmin nearly in the plane containing the Cassini state. The core spin lags the precessing plane containing the Cassini state by an increasing angle as the core viscosity is increased. With the maximum viscosity considered of  $\nu \sim 15.0 \text{ cm}^2/\text{s}$  if the coupling is by the circulation through an Ekman boundary layer or  $\nu \sim 8.75 \times 10^5 \text{ cm}^2/\text{s}$  for purely viscous coupling, the core spin lags the precessing Cassini plane by 23 arcsec, whereas the mantle spin lags by only 0.055 arcsec. Larger, non hydrostatic values of the CMB ellipticity also result in the mantle spin at the Cassini state, but the core spin is moved closer to the mantle spin. Current measurement uncertainties preclude using the mantle offset to constrain the internal core viscosity.

## 1. Introduction

Mercury is in a stable spin–orbit resonance in which the rotational angular velocity is precisely 1.5 times the mean orbital motion (Pettengill and Dyce, 1965; Colombo and Shapiro, 1966). This rotation state is a natural outcome of tidal evolution (Goldreich and Peale, 1966; Correia and Laskar, 2004, 2009). In addition, the same tidal evolution brings Mercury to Cassini state 1, wherein Mercury’s spin axis remains coplanar with the orbit normal and Laplace plane normal as the spin vector and orbit normal precess around the latter with a  $\sim 300,000$  yr period (Colombo 1966, Peale, 1969, 1974). That Mercury is very close to this state has been verified with radar observations, which give an obliquity of  $2.04 \pm 0.08$  arcmin (Margot *et al.*, 2007, 2012). The most recent observations show that the best-fit solution is offset from the Cassini state by a few arcseconds, but the uncertainty at one standard deviation includes the Cassini state.

This paper is an investigation of the possible displacement of the spin axis from the Cassini state from dissipative processes and the consequences of pressure coupling. In Section 2 we develop the equations for the rotational motion of both the core and mantle plus crust from conservative and dissipative torques. The latter include the tidal torque and the torques due to viscous, magnetic, and topographical coupling between the core and the mantle plus crust for a spherically symmetric core–mantle boundary (CMB). Gravitational and rotational distortions of the CMB lead to pressure torques that dominate all the dissipative torques. Results are given in Section 3, where we show that the tidal offset of the mantle spin axis from the Cassini state is immeasurably small, but the offset due to the core–mantle interactions can be quite large, and weaker core–mantle coupling leads to larger offsets. The core–mantle dissipative coupling must be relatively strong to bring the mantle spin–axis to within the uncertainty of its observed location. The failure of viscous, magnetic and topographic mechanisms, which dominate the tidal mechanism, to bring the spin axis near its observed position for measured or likely values of the parameters is compensated by the pressure coupling between the core and mantle for both hydrostatic and non–hydrostatic ellipsoidal CMB, which we examine in Section 3.5.

We maintain the current orbital configurations throughout the calculations even though the dissipative time scales are long enough for significant changes to occur. This assumption is justified because the spin axis will follow the Cassini state as the latter’s position changes during the slow changes in the solar system configuration because of adiabatic invariance of the solid angle swept out by the spin axis as it precesses around the Cassini state. The spin axis remains within 1 arcsec of the Cassini state position through both long-period and short-period changes in the state position (Peale, 2006). We are interested only in the final equilibrium positions of the core and mantle spins in the current orbit frame of reference, and these positions will be the same if the evolution takes place with the current, fixed orbital and solar system parameters or if these parameters are allowed to evolve during the evolution to the current state.

## 2. Equations of variation

The coordinate systems and angles for the equations that govern the rotational motion of Mercury are shown in Fig. 1, where  $X', Y', Z'$  are quasi-inertial axes with the  $X'Y'$  plane being the Laplace plane on which Mercury's orbit precesses at nearly a constant inclination  $I$  and nearly constant angular velocity  $\mu$ . The  $XYZ$  orbit system has the  $X$  axis along the ascending node of the orbit plane on the Laplace plane, and the  $XY$  plane is the orbit plane. The  $xyz$  system is fixed in the body, with  $z$  along the spin axis and  $x$  along the the axis of minimum moment of inertia in the equator plane. The Euler angles orienting the  $xyz$  system relative to the  $XYZ$  system are  $\Omega, i, \psi$ , where  $\Omega$  is the longitude of the ascending node of the equator plane on the  $XY$  orbit plane measured from the  $X$  axis,  $i$  is the inclination of the equator plane to the orbit plane, and  $\psi$  is the angle from the ascending node of the equator on the orbit plane to the  $x$  axis of minimum moment of inertia. The three Euler angles will have subscripts  $m$  or  $f$  to designate mantle or fluid core, respectively. Angle  $I$  is the inclination of the orbit plane to the Laplace plane,  $\Omega_o$  is the longitude of the ascending node of the orbit plane on the Laplace plane,  $\omega$  is the argument of perihelion,  $f$  is the true anomaly of the Sun, and  $r$  is the distance from Mercury to the Sun.

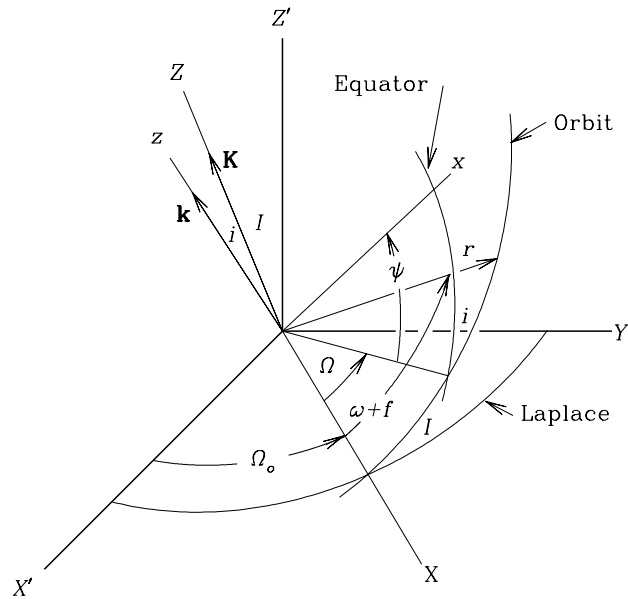


Fig. 1.— Coordinate systems and relevant angles. The angles orienting mantle or core relative to the  $XYZ$  orbit system will have subscripts  $m$  or  $c$ , respectively.

We assume principal axis rotation throughout. The angular momentum of the mantle plus crust is  $\mathbf{L}_m = C_m \dot{\psi}_m \mathbf{k}_m = C_m \dot{\psi}_m$ , where  $C_m$  is the moment of inertia of the mantle plus crust about the spin axis,  $\dot{\psi}_m$  is the angular velocity of the mantle, and  $\mathbf{k}_m = \sin i_m \sin \Omega_m \mathbf{I} - \sin i_m \cos \Omega_m \mathbf{J} + \cos i_m \mathbf{K}$  is a unit vector along the spin axis.  $\mathbf{I}, \mathbf{J}, \mathbf{K}$  are unit vectors along the  $X, Y, Z$  axes, respectively. With  $d\mathbf{L}_m/dt = C_m(d\dot{\psi}_m/dt)\mathbf{k}_m + C_m\dot{\psi}_m(d\mathbf{k}_m/dt)$ , we can write

$$\begin{aligned} \frac{1}{C_m} \frac{dL_{mx}}{dt} &= \frac{d\dot{\psi}_m}{dt} \sin i_m \sin \Omega_m + \dot{\psi}_m \left[ \cos i_m \sin \Omega_m \frac{di_m}{dt} + \sin i_m \cos \Omega_m \frac{d\Omega_m}{dt} \right] \\ \frac{1}{C_m} \frac{dL_{my}}{dt} &= -\frac{d\dot{\psi}_m}{dt} \sin i_m \cos \Omega_m + \dot{\psi}_m \left[ -\cos i_m \cos \Omega_m \frac{di_m}{dt} + \sin i_m \sin \Omega_m \frac{d\Omega_m}{dt} \right] \\ \frac{1}{C_m} \frac{dL_{mz}}{dt} &= \frac{d\dot{\psi}_m}{dt} \cos i_m - \dot{\psi}_m \sin i_m \frac{di_m}{dt} \end{aligned} \quad (1)$$

for the variations of the three components of angular momentum relative to the orbit system of coordinates, which system is readily observable.

The total torque on Mercury’s mantle plus crust,  $\langle \mathbf{T}_m \rangle = \langle \mathbf{T}_{body} \rangle + \langle \mathbf{T}_{tide} \rangle + \langle \mathbf{T}_{f-m} \rangle$ , is the sum of the conservative gravitational torque, the tidal torque, and the torque from the core–mantle interaction. The latter torque has four contributions,  $\langle \mathbf{T}_{viscous} \rangle$ ,  $\langle \mathbf{T}_{magnetic} \rangle$ ,  $\langle \mathbf{T}_{topographic} \rangle$ , and  $\langle \mathbf{T}_{pressure} \rangle$ , for viscous, magnetic, topographic, and pressure coupling, respectively. The angled brackets indicate that these torques are averaged over an orbit period; the core–mantle torques do not involve the orbital elements, so they are intrinsically averaged. We desire the variation of  $\mathbf{L}_m$  relative to the precessing orbit system, where the variation relative to inertial space is given by the total torque. We therefore write  $d\mathbf{L}_m/dt = \langle \mathbf{T}_m \rangle - \boldsymbol{\mu} \times \mathbf{L}_m$ , where  $\boldsymbol{\mu}$  is the angular velocity of the orbit precession. If we write  $\mathbf{N}_m = \langle \mathbf{T}_m \rangle / C_m - \boldsymbol{\mu} \times \dot{\psi}_m$ , we can equate each component of  $(1/C_m)d\mathbf{L}_m/dt$  in Eqs. (1) to the corresponding component of  $\mathbf{N}_m$  and solve the resulting set for  $d\dot{\psi}_m/dt$ ,  $di_m/dt$ , and  $d\Omega_m/dt$  to follow the motion of Mercury’s mantle under conservative and dissipative torques. We find

$$\begin{aligned} \frac{d\dot{\psi}_m}{dt} &= \sin i_m (N_{mx} \sin \Omega_m - N_{my} \cos \Omega_m) + N_{mz} \cos i_m, \\ \frac{di_m}{dt} &= -\frac{1}{\dot{\psi}_m} [\cos i_m (-N_{mx} \sin \Omega_m + N_{my} \cos \Omega_m) + N_{mz} \sin i_m], \\ \frac{d\Omega_m}{dt} &= \frac{1}{\dot{\psi}_m \sin i_m} (N_{mx} \cos \Omega_m + N_{my} \sin \Omega_m). \end{aligned} \quad (2)$$

We change variables to  $p_m = \sin i_m \sin \Omega_m$  and  $q_m = \sin i_m \cos \Omega_m$  to eliminate the  $\sin i_m$  singularity in the third of Eqs. (2). Differentiating these variables with respect to time, substituting the expressions for the time derivatives from Eqs. (2), and expressing the circular functions in terms of  $p_m$  and  $q_m$  yields

$$\begin{aligned} \frac{d\dot{\psi}_m}{dt} &= p_m N_{mx} - q_m N_{my} + \sqrt{1 - p_m^2 - q_m^2} N_{mz} \\ \frac{dp_m}{dt} &= \frac{1}{\dot{\psi}_m} \left[ (1 - p_m^2) N_{mx} + p_m q_m N_{my} - p_m \sqrt{1 - p_m^2 - q_m^2} N_{mz} \right] \\ \frac{dq_m}{dt} &= -\frac{1}{\dot{\psi}_m} \left[ p_m q_m N_{mx} + (1 - q_m^2) N_{my} + q_m \sqrt{1 - p_m^2 - q_m^2} N_{mz} \right] \end{aligned} \quad (3)$$

as the equations to be solved for the behavior of the mantle under the applied torques. The corresponding equations for the core are identical to Eqs. (3) with all the  $m$  subscripts replaced by  $f$ . Now we must construct the expressions for  $\langle \mathbf{T}_{body} \rangle$ ,  $\langle \mathbf{T}_{tide} \rangle$ ,  $\langle \mathbf{T}_{viscous} \rangle$ ,  $\langle \mathbf{T}_{magnetic} \rangle$ ,  $\langle \mathbf{T}_{topographic} \rangle$ , and  $\langle \mathbf{T}_{pressure} \rangle$  in terms of the variables of Eqs. (3).

## 2.1. Conservative gravitational torque

The conservative body torque the Sun exerts on Mercury is  $\mathbf{T}_{body} = \mathbf{r} \times \nabla V$ , where

$$V = -\frac{G m m_{\odot}}{r} \left[ 1 - J_2 \frac{R^2}{r^2} \left( \frac{3 \cos^2 \theta}{2} - \frac{1}{2} \right) + 3C_{22} \frac{R^2}{r^2} \sin^2 \theta \cos 2\phi \right] \quad (4)$$

is the potential energy of the Sun in Mercury's gravitational field up to second spherical harmonic degree, and  $\mathbf{r}$  is the vector from Mercury to the Sun. In Eq. (4),  $m$  and  $m_{\odot}$  are the masses of Mercury and the Sun, respectively,  $G$  is the gravitational constant,  $R$  is Mercury's radius,  $\theta$  and  $\phi$  are spherical polar coordinates relative to Mercury's principal axis system of coordinates, which define the direction to the Sun, and  $J_2 = [C - (A + B)/2]/m R^2$  and  $C_{22} = (B - A)/4m R^2$  are unnormalized zonal and tesseral coefficients of degree 2 in the spherical harmonic expansion of Mercury's gravitational potential.  $A < B < C$  are principal moments of inertia of Mercury. It is expedient to form the cross product in the body system of coordinates and express the resulting combinations of the spherical polar coordinates in terms of scalar products to yield

$$\begin{aligned} (\mathbf{r} \times \nabla V)_x &= \frac{G m m_{\odot} R^2}{r^5} (\mathbf{r} \cdot \mathbf{k})(\mathbf{r} \cdot \mathbf{j})(3J_2 - 6C_{22}), \\ (\mathbf{r} \times \nabla V)_y &= -\frac{G m m_{\odot} R^2}{r^5} (\mathbf{r} \cdot \mathbf{k})(\mathbf{r} \cdot \mathbf{i})(3J_2 + 6C_{22}), \\ (\mathbf{r} \times \nabla V)_z &= 12 \frac{G m m_{\odot} R^2}{r^5} (\mathbf{r} \cdot \mathbf{i})(\mathbf{r} \cdot \mathbf{j})C_{22}, \end{aligned} \quad (5)$$

where  $\mathbf{i}, \mathbf{j}, \mathbf{k}$  are unit vectors along the  $x, y, z$  axes, respectively. The components of  $\mathbf{T}_{body}$  in the  $XYZ$  orbit system are obtained by rotations through the Euler angles  $\Omega_m, i_m, \psi_m$  defined in Fig. 1, where the scalar products in Eqs. (5) are also expressed in terms of their  $XYZ$  components. Then

$$\begin{aligned} \mathbf{T}_{body} &= -\frac{G m m_{\odot} R^2}{r^3} \left\{ 3J_2 \sin i_m \cos i_m \sin(\omega + f - \Omega_m) [\sin(\omega + f)\mathbf{I} - \cos(\omega + f)\mathbf{J}] \right. \\ &\quad - 1.5J_2 \sin^2 i_m \sin 2(\omega + f - \Omega_m)\mathbf{K} + \\ &\quad 6C_{22} \sin i_m [\cos i_m \cos 2\psi_m \sin(\omega + f - \Omega_m) - \sin 2\psi_m \cos(\omega + f - \Omega_m)] \times \\ &\quad \left. [-\sin(\omega + f)\mathbf{I} + \cos(\omega + f)\mathbf{J}] + \right. \\ &\quad \left. 6C_{22} \left[ -\left( \frac{3 + \cos 2i_m}{4} \right) \cos 2\psi_m \sin 2(\omega + f - \Omega_m) + \cos i_m \sin 2\psi_m \cos 2(\omega + f - \Omega_m) \right] \mathbf{K} \right\}, \end{aligned} \quad (6)$$

which is identical to Eq. (7) of Peale (2005) with  $f$  replaced by  $\omega + f$  ( $\omega = 0$  in the 2005 paper).

The average over the orbit is carried out by keeping all slowly varying parameters constant, while the true anomaly and rotation are allowed to vary. With Mercury in the 3:2 spin orbit resonance,  $\dot{\psi} = 1.5n + \dot{\gamma}$ , where  $\dot{\gamma}$  allows a small variation in the rotation rate relative to the resonant

value. The stability of the resonance requires the axis of minimum moment of inertia (long axis) to be nearly aligned with the direction to the Sun when Mercury is at perihelion. A slight deviation from this condition will cause a free libration about this position that will be damped by dissipation. We can represent the position of the long axis by  $\psi_m = 1.5M + \omega - \Omega_m + \gamma$  from inspection of Fig. 1, where  $\omega - \Omega_m$  is the angular distance from the ascending node of the equator on the orbit plane to the perihelion with  $i_m \ll 1$ , and  $M$  is the mean anomaly. The variations of  $\omega$  and  $\Omega$  are sufficiently slow that they can be ignored on the orbital and rotation time scales. At perihelion,  $M = 0$ , so  $\gamma$  is a small offset of the long axis from the direction to the Sun when Mercury is at perihelion. For the averaging procedure,  $2\psi_m = 3M + 2(\omega - \Omega_m) + 2\gamma$ . The rapidly varying quantities in Eq. (6) are thus  $f$ ,  $M$ , and  $r$  in terms which can be isolated by expanding the circular functions. Non-zero averages of  $a^3/r^3$ ,  $(a^3/r^3)\cos 2f \cos 3M$ ,  $(a^3/r^3)\sin 2f \sin 3M$ , and  $(a^3/r^3)\cos 3M$ , where  $a$  is the semimajor axis of Mercury's orbit, are expressed as series in the orbital eccentricity  $e$ , where we truncate each series at  $e^5$ . After some algebraic manipulation and combination of terms, we find the averaged torque to be

$$\begin{aligned}
 \frac{\langle \mathbf{T}_{body} \rangle_x}{C_m} &= -\frac{n^2}{\alpha_m} \left[ \frac{3}{2} J_2 \sin i_m \cos i_m \cos \Omega_m g_1(e) \right. \\
 &\quad + \frac{3}{2} C_{22} \sin i_m (1 + \cos i_m) \cos(\Omega_m - 2\gamma) g_2(e) \\
 &\quad \left. + \frac{3}{2} C_{22} \sin i_m (1 + \cos i_m) \cos(2\omega - \Omega_m + 2\gamma) g_3(e) \right], \\
 \frac{\langle \mathbf{T}_{body} \rangle_y}{C_m} &= -\frac{n^2}{\alpha_m} \left[ \frac{3}{2} J_2 \sin i_m \cos i_m \sin \Omega_m g_1(e) \right. \\
 &\quad + \frac{3}{2} C_{22} \sin i_m (1 + \cos i_m) \sin(\Omega_m - 2\gamma) g_2(e) \\
 &\quad \left. - \frac{3}{2} C_{22} \sin i_m (1 + \cos i_m) \sin(2\omega - \Omega_m + 2\gamma) g_3(e) \right], \\
 \frac{\langle \mathbf{T}_{body} \rangle_z}{C_m} &= -\frac{n^2}{\alpha_m} \left\{ \frac{3}{2} C_{22} (1 + \cos i_m)^2 \left[ g_2(e) \sin 2\gamma + g_4(e) \sin(4\omega - 4\Omega_m + 2\gamma) \right] \right\}, \quad (7)
 \end{aligned}$$

where  $C_m = \alpha_m m R^2$  defines  $\alpha_m$ , and  $n^2 = Gm_\odot/a^3$  has been used. The choice of  $C_m$  in Eqs. (7) means they apply to the mantle alone, and  $J_2$  and  $C_{22}$  correspond only to this part of Mercury. We show in Section 2.6 and Appendix B that pressure torques effectively restore the full values of  $J_2$  and  $C_{22}$  in these equations. In Eqs. (7)

$$\begin{aligned}
 g_1(e) &= (1 - e^2)^{-3/2} \\
 g_2(e) &= \frac{7e}{2} - \frac{123e^3}{16} + \frac{489e^5}{128} + \dots \\
 g_3(e) &= \frac{53e^3}{16} + \frac{393e^5}{256} + \dots \\
 g_4(e) &= \frac{85e^5}{2560} + \dots \quad (8)
 \end{aligned}$$

There are additional terms in the  $X$  and  $Y$  components of  $\mathbf{T}_{body}$  to order  $e^5$  with factors  $\sin i_m (1 - \cos i_m)$ . Since Mercury's obliquity is about 2 arcmin (Margot *et al.*, 2007, 2012) and since we al-

ways start the integrations close to the final state, these factors coupled with lowest-order factors of  $e^3$  or  $e^5$  make these terms negligibly small compared with the terms that are retained. With core parameters, Eqs. (7) apply to the core as well, but we show below that pressure forces between core and mantle effectively cancel the gravitational torque on the core.

## 2.2. Tidal torque

We choose the simplest tidal model, in which an equilibrium tidal distortion has its maximum displacement at a point that was directly under the disturbing body, here the Sun, a short time  $\Delta t$  in the past. This model is equivalent to setting the tidal dissipation factor  $Q$  inversely proportional to frequency. This model is not a good representation of the behavior of solid materials (Castillo-Rogez *et al.*, 2011), but since the frequencies involved will be near the orbital frequency  $n$  and are confined to a fairly narrow range, we expect that the time scale for evolution to equilibrium will depend more on the value of  $Q$  than on the tidal model. We are interested in the final equilibrium state and not necessarily in the rate of approach. It can be shown that for a tidal frequency equal to the orbital mean motion  $n$ ,  $\Delta t = 1/(Qn)$ , where  $Q$  has the value appropriate to a tidal frequency  $n$  (e.g., Peale 2005, 2006). There are many treatments in which this model is developed and used (e.g., Mignard 1979, 1980, 1981; Hut 1981; Peale 2005, 2007). Peale (2005) derived the tidal torque averaged over an orbit period for the case where the argument of periape  $\omega$  is set to zero. The averaged equations must be re-derived by procedures in the 2005 paper to include non-zero values of  $\omega$ . We find

$$\begin{aligned} \frac{\langle \mathbf{T}_{tide} \rangle}{C_m} = & 3 \frac{n^2 m_\odot R^3}{\alpha_m m a^3} k_2 \Delta t \left\{ -\dot{\psi}_m \left[ p_m \frac{f_2(e)}{2} + (q_m \sin 2\omega - p_m \cos 2\omega) \frac{f_3(e)}{2} \right] \mathbf{I} \right. \\ & + \dot{\psi}_m \left[ q_m \frac{f_2(e)}{2} + (q_m \cos 2\omega + p_m \sin 2\omega) \frac{f_3(e)}{2} \right] \mathbf{J} \\ & \left. + \left[ n f_1(e) - f_2(e) \dot{\psi}_m \sqrt{1 - p_m^2 - q_m^2} \right] \mathbf{K} \right\} \end{aligned} \quad (9)$$

where  $k_2$  is the second-degree potential Love number, and where we have converted the circular functions in the expressions to our variables  $p_m$  and  $q_m$ . In Eqs. (9)

$$\begin{aligned} f_1(e) &= \left( 1 + \frac{15e^2}{2} + \frac{45e^4}{8} + \frac{5e^6}{16} \right) / (1 - e^2)^6 \\ f_2(e) &= \left( 1 + 3e^2 + \frac{3e^4}{8} \right) / (1 - e^2)^{9/2} \\ f_3(e) &= \left( \frac{3e^2}{2} + \frac{e^4}{4} \right) / (1 - e^2)^{9/2} \end{aligned} \quad (10)$$

### 2.3. Viscous core–mantle torque

For the viscous interaction between the core and mantle we assume that the torque is simply proportional to the difference in the vector angular velocities. This assumption is consistent with the core rotating as a rigid body (Poincaré, 1910).

$$\begin{aligned}\langle \mathbf{T}_{viscous}^m \rangle &= -\beta(\dot{\boldsymbol{\psi}}_m - \dot{\boldsymbol{\psi}}_f), \\ \langle \mathbf{T}_{viscous}^f \rangle &= -\langle \mathbf{T}_{viscous}^m \rangle\end{aligned}\quad (11)$$

are the torques on the mantle and core, respectively. Since the core–mantle torques do not change with orbital position, the averaged values are the same as the defining expressions. If we assume that the angular velocities are parallel and that the torques in Eqs. (11) are the only ones acting, the time constant for an exponential decay of the differential rotation is  $C_f C_m / [\beta(C_f + C_m)]$ , which follows from the difference in the angular momentum equations for the mantle and core appropriate to the above torques. We connect  $\beta$  to the viscosity of the fluid by equating this time constant to that for the decay of fluid rotation relative to its container. We thereby restore the effects of the fluid nature of the core. If the viscosity is small, a time scale for damping the rotation of the core relative to the CMB is  $R_f / (\dot{\psi} \nu)^{1/2}$  (Greenspan and Howard, 1963), where  $\nu$  is the kinematic viscosity, and  $R_f$  is the radius of the fluid core. The time scale is derived for no density stratification in the core and depends on circulation of the fluid through the Ekman boundary layer, the thickness of which is small compared with the core radius. If the viscosity is large, the latter condition is not necessarily satisfied, and the viscous time scale  $R_f^2 / \nu$  becomes appropriate. It is probably unlikely that the viscosity of the liquid core material is uniform throughout or that there is no density stratification therein. A purely viscous time scale using the viscosity at the CMB may therefore be more appropriate than the Greenspan and Howard time scale, but we determine the dependence of the coupling constant  $\beta$  on the liquid core viscosity for both possibilities.

$$\beta = \frac{(\dot{\psi} \nu)^{1/2}}{R_f} \frac{C_f C_m}{C_f + C_m} \quad (12)$$

or

$$\beta = \frac{\nu}{R_f^2} \frac{C_f C_m}{C_f + C_m} \quad (13)$$

for small and large viscosities, respectively. With  $\dot{\boldsymbol{\psi}}_m = \dot{\psi}_m \mathbf{k}_m = \dot{\psi}_m [p_m \mathbf{I} - q_m \mathbf{J} + \sqrt{1 - p_m^2 - q_m^2} \mathbf{K}]$  and with a similar expression for  $\dot{\boldsymbol{\psi}}_f$ , we can write

$$\begin{aligned}\langle T_{viscous}^m \rangle_x &= -\beta(p_m \dot{\psi}_m - p_f \dot{\psi}_f), \\ \langle T_{viscous}^m \rangle_y &= -\beta(-q_m \dot{\psi}_m + q_f \dot{\psi}_f), \\ \langle T_{viscous}^m \rangle_z &= -\beta \left( \dot{\psi}_m \sqrt{1 - p_m^2 - q_m^2} - \dot{\psi}_f \sqrt{1 - p_f^2 - q_f^2} \right),\end{aligned}\quad (14)$$

where the same equations give the components of  $\langle \mathbf{T}_{viscous}^f \rangle$  but with the leading signs reversed.

## 2.4. Magnetic core–mantle torque

An expression for the magnetic torque on the mantle is given by Buffett (1992).

$$\mathbf{T}_{magnetic} = \frac{|\Phi_B|}{\mu_0} \int_S [B_r(r)]^2 [r^2 \mathbf{w} - (\mathbf{r} \cdot \mathbf{w}) \mathbf{r}] dS, \quad (15)$$

where the integral is over the CMB and where  $\mathbf{w} = \dot{\boldsymbol{\psi}}_m - \dot{\boldsymbol{\psi}}_f$  is the relative angular velocity between the mantle and core,  $B_r(r)$  is the radial component of the magnetic field at the CMB,  $|\Phi_B| \approx 43$  s/m when the thickness of the conducting layer in the mantle exceeds 200 m with conductivity  $\sigma = 5 \times 10^5$  S/m appropriate to Buffett's assumed properties of the Earth's mantle at the CMB, and  $\mu_0 = 4\pi \times 10^{-7}$  N/A<sup>2</sup> is the permeability of free space. The magnetic torque will of course change with different values of the thickness of the conducting layer and electrical conductivity, but the changes in  $|\Phi_B|$  are easily determined within the Buffett (1992) theory.

The magnetic field of Mercury is primarily a spin–aligned dipole, for which the radial component is given by

$$B_r(r, \theta) = \frac{\mu_0 \mathcal{M} \cos \theta}{2\pi r^3}, \quad (16)$$

where  $\theta$  is the co-latitude and  $\mathcal{M}$  is the magnetic dipole moment. The dipole is here centered at the origin of the coordinate system. But the center of the Mercury's dipole is offset northward from the center of the planet by 486 km (Anderson *et al.* 2011, 2012), and this offset complicates the calculation of  $B_r$  relative to the center of Mercury. We calculate the magnetic torque evolution of the system for a Mercury-centered dipole, with straightforward integration over the CMB. With  $\mathbf{r} = R_f \hat{\mathbf{r}}$ , where  $\hat{\mathbf{r}}$  is a unit vector in the direction of  $\mathbf{r}$ , substitution of Eq. (16) into Eq. (15) yields

$$\mathbf{T}_{magnetic} = \frac{|\Phi_B| \mu_0 \mathcal{M}^2}{4\pi^2 R_f^2} \int_0^{2\pi} \int_0^\pi [\mathbf{w} - (\hat{\mathbf{r}} \cdot \mathbf{w}) \hat{\mathbf{r}}] \cos^2 \theta \sin \theta d\theta d\phi, \quad (17)$$

where  $\theta$  and  $\phi$  are spherical polar coordinates of a point on the CMB in the body xyz system. The relative angular velocity  $\mathbf{w}$  remains constant for the integration over the CMB. We find

$$\mathbf{T}_{magnetic} = \frac{|\Phi_B| \mu_0 \mathcal{M}^2}{15\pi R_f^2} [4(w_x \mathbf{i} + w_y \mathbf{j} + w_z \mathbf{k}) - 2w_z \mathbf{k}], \quad (18)$$

where  $\mathbf{i}, \mathbf{j}, \mathbf{k}$  are unit vectors along the xyz body axes, respectively. The vector  $\mathbf{w}$  in Eq. (18) is just  $\dot{\boldsymbol{\psi}}_m - \dot{\boldsymbol{\psi}}_f$  which can be expressed in the XYZ orbit system, and the last term is just  $2(\mathbf{w} \cdot \mathbf{k}_m) \mathbf{k}_m$ , which is also expressible in the XYZ system. (Recall that  $\mathbf{k}_m = p_m \mathbf{I} - q_m \mathbf{J} + \sqrt{1 - p_m^2 - q_m^2} \mathbf{K}$ .) There results

$$T_{magnetic}^x = \frac{|\Phi_B| \mu_0 \mathcal{M}^2}{15\pi R_f^2} \left\{ 4(p_m \dot{\psi}_m - p_f \dot{\psi}_f) - 2p_m \left[ (p_m \dot{\psi}_m - p_f \dot{\psi}_f) p_m + (q_m \dot{\psi}_m - q_f \dot{\psi}_f) q_m + \left( \sqrt{1 - p_m^2 - q_m^2} \dot{\psi}_m - \sqrt{1 - p_f^2 - q_f^2} \dot{\psi}_f \right) \sqrt{1 - p_m^2 - q_m^2} \right] \right\}$$

$$\begin{aligned}
 T_{magnetic}^y &= \frac{|\Phi_B| \mu_0 \mathcal{M}^2}{15\pi R_f^2} \left\{ -4(q_m \dot{\psi}_m - q_f \dot{\psi}_f) + 2q_m \left[ (p_m \dot{\psi}_m - p_f \dot{\psi}_f) p_m + (q_m \dot{\psi}_m - q_f \dot{\psi}_f) q_m + \right. \right. \\
 &\quad \left. \left. \left( \sqrt{1 - p_m^2 - q_m^2} \dot{\psi}_m - \sqrt{1 - p_f^2 - q_f^2} \dot{\psi}_f \right) \sqrt{1 - p_m^2 - q_m^2} \right] \right\} \\
 T_{magnetic}^z &= \frac{|\Phi_B| \mu_0 \mathcal{M}^2}{15\pi R_f^2} \left\{ 4 \left( \sqrt{1 - p_m^2 - q_m^2} \dot{\psi}_m - \sqrt{1 - p_f^2 - q_f^2} \dot{\psi}_f \right) - \right. \\
 &\quad 2\sqrt{1 - p_m^2 - q_m^2} \left[ (p_m \dot{\psi}_m - p_f \dot{\psi}_f) p_m + (q_m \dot{\psi}_m - q_f \dot{\psi}_f) q_m + \right. \\
 &\quad \left. \left. \left( \sqrt{1 - p_m^2 - q_m^2} \dot{\psi}_m - \sqrt{1 - p_f^2 - q_f^2} \dot{\psi}_f \right) \sqrt{1 - p_m^2 - q_m^2} \right] \right\} \quad (19)
 \end{aligned}$$

## 2.5. Topographic core–mantle torque

The differential rotation of the mantle and core can lead to dynamic pressure forces on any topography on the CMB. The form of the torque on topography starts with the dynamic pressure of a fluid times the area element  $\rho u^2 dS$ , where  $u$  is the magnitude of a relative velocity, and  $\rho$  is a fluid density. This gives a force on  $dS$  as if the relative fluid velocity were impinging on the CMB in the normal direction. If the vertical extent of the bump that occupies area element  $dS$  on the CMB leads to a cross section as seen by the fluid that is flowing parallel to the mean CMB surface of  $dS \sin \delta$ , where angle  $\delta$  is the slope of the bump relative to the mean CMB, the dynamic force on the bump is  $\rho u^2 \sin \delta dS$ . But this element of surface results not from a face perpendicular to the flow but from the projection of the slanted surface perpendicular to the direction of  $\mathbf{u}$ . So a factor  $\zeta < 1$  is inserted as an unknown efficiency of the transfer of linear momentum to the slanted surface. The efficiency factor  $\zeta$  is difficult to estimate, so we leave it as a parameter.

If the velocity of the CMB relative to the fluid is represented by  $\mathbf{u} = (\dot{\psi}_m - \dot{\psi}_f) \times \mathbf{R}_f$ , and  $\sin \delta = |\hat{\mathbf{r}} \times \hat{\mathbf{n}}|$ , with  $\hat{\mathbf{n}}$  a unit vector normal to the CMB surface at  $(R_f, \theta, \phi)$  and  $\hat{\mathbf{r}}$  a unit vector in the direction of  $\mathbf{r}$ , then the increment of topographic pressure force on the mantle is

$$-\rho_f u \zeta \sin \delta dS \mathbf{u}, \quad (20)$$

where  $\rho_f$  is the density of the liquid core at the CMB. If the surface is spherical, the stress is zero. (We do not consider the effect of the ellipsoidal mean surface here.) The force  $d\mathbf{F}$  on the mantle from the stress on an area  $dS$  is in the direction of  $-\mathbf{u}$ , and the torque on the mantle from  $d\mathbf{F}$  is  $\mathbf{R}_f \times d\mathbf{F}$ .

The total torque on the mantle from topography on the CMB is then

$$\mathbf{T}_{topographic} = - \int_0^{2\pi} \int_0^\pi \zeta \sin \delta \rho_f u \mathbf{R}_f \times \mathbf{u} R_f^2 \sin \theta d\theta d\phi. \quad (21)$$

In the integrand of Eq. (21),  $u = \sqrt{\mathbf{u} \cdot \mathbf{u}}$  prohibits the analytic integration over the CMB. However, with  $\dot{\psi}_m = \dot{\psi}_m (p_m \mathbf{I} - q_m \mathbf{J} + \sqrt{1 - p_m^2 - q_m^2} \mathbf{K})$  and a similar expression for  $\dot{\psi}_f$ , and with the

components of  $\mathbf{R}_f$  in the same system of coordinates expressed in spherical polar coordinates, it is easy to express  $u^2$  in terms of the  $p$ s and  $q$ s and  $\theta$  and  $\phi$ . If we limit ourselves to small obliquities in the final evolution of the system to equilibrium, then  $p_m, q_m, p_f, q_f \ll 1$ . With these quantities set to zero in the expression for  $u^2$ , we have  $u \approx R_f |\dot{\psi}_m - \dot{\psi}_f| \sin \theta$  and Eq. (21) is integrable to yield

$$\begin{aligned} \frac{T_{topographic}^x}{C_m} &= -\chi |\dot{\psi}_m - \dot{\psi}_f| (p_m \dot{\psi}_m - p_f \dot{\psi}_f), \\ \frac{T_{topographic}^y}{C_m} &= \chi |\dot{\psi}_m - \dot{\psi}_f| (q_m \dot{\psi}_m - q_f \dot{\psi}_f), \\ \frac{T_{topographic}^z}{C_m} &= -2\chi |\dot{\psi}_m - \dot{\psi}_f| (\sqrt{1 - p_m^2 - q_m^2} \dot{\psi}_m - \sqrt{1 - p_f^2 - q_f^2} \dot{\psi}_f), \end{aligned} \quad (22)$$

where  $\chi = 5\zeta \sin \delta \pi^2 \rho_f R_f^5 / (16\alpha_m m R^2) = (15/64)(m_f/m)(1/\alpha_m)(R_f^2/R^2)\pi\zeta \sin \delta = 2.4301\zeta \sin \delta$ , with  $m_f/m = 0.7334$ ,  $R_f = 1998\text{km}$ , and  $\alpha_m = 0.149$  for the two-layer model discussed in the next section. We have assumed that the “roughness” of the CMB is the same everywhere such that  $\zeta \sin \delta$  is a constant.

## 2.6. Pressure torque

The influence of pressure torques at the CMB on Mercury’s libration in longitude have been considered by Van Hoolst *et al.* (2012). Here we generalize the pressure torques to three dimensions, where variations in fluid velocity are important. Until now we have ignored the presence of the solid inner core, and we will ultimately determine the pressure torque for an entirely fluid core. However, in determining the shape of the CMB as an equipotential surface, it is convenient to also determine the shape of the inner core boundary (ICB) as a function of the inner core size and density. We will use the shape of the ICB in a later work determining the equilibrium spin of the inner core and its gravitational effect on the mantle spin. We therefore model the interior structure of Mercury as three homogeneous layers, mantle plus crust, fluid outer core, and solid inner core. The observed values of  $J_2$  and  $C_{22}$  can be expressed as a sum of contributions from the ellipsoidal shapes of the surfaces of each layer. For principal axes of the ellipsoids given by  $a > b > c$  and principal moments of inertia  $A < B < C$ ,  $J_2$  is expressed in terms of the mean polar ellipticities  $\epsilon = (\epsilon_a + \epsilon_b)/2 = [(a - c)/r_0 + (b - c)/r_0]/2$  ( $r_0 = \text{mean radius}$ ), the surface radii  $R_m = R, R_f$ , and  $R_s$  ( $R_s$  is the solid inner core radius), and the densities of the layers,  $\rho_m, \rho_f$ , and  $\rho_s$ .  $C_{22}$  is expressed in terms of the equatorial ellipticities  $\xi = (a - b)/r_0$ , the densities, and the surface radii. The subscripts  $m, f$ , and  $s$  refer to the mantle, fluid outer core, and solid inner core, respectively. Additional equations in these same variables are determined by the assumption of hydrostatic equilibrium, where the CMB and the inner core boundary (ICB) are equipotential surfaces. In computing the gravitational potential throughout the interior of the planet, we assume that the surfaces have the form

$$r = r_0 \left[ 1 - \frac{2\epsilon}{3} P_{20}(\cos \theta) + \frac{\xi}{6} P_{22}(\cos \theta) \cos 2\phi \right], \quad (23)$$

where  $P_{ij}$  are Legendre functions, and  $\theta$  and  $\phi$  are spherical polar coordinates ( $\theta = \text{colatitude}$ ) relative to the principal axis system in which the  $x$  axis is the axis of minimum moment of inertia (semiaxis  $a$ ). The coefficients of the Legendre functions in Eq. (23) are determined by evaluating coefficients  $\Delta R_1/r_0$  and  $\Delta R_2/r_0$  of the two Legendre functions by setting  $r = a, b$ , and  $c$  for appropriate choices of the angles therein and solving for the  $\Delta R_i$  in terms of differences in the axis lengths expressed by  $\epsilon$  and  $\xi$ .

The equipotential surfaces at the CMB and ICB give two equations in  $\epsilon_i$  and  $\xi_i$ , which can be decomposed into equations for the  $\epsilon_i$  and separately for the  $\xi_i$  because of the orthogonality of the Legendre functions.  $J_2$  and the equations of two equipotential surfaces involving the polar ellipticities  $\epsilon_i$  comprise three equations with additional parameters,  $\rho_i$  and  $R_i$ . Similarly, three equations are found for  $C_{22}$  and two equipotential surfaces involving  $\xi_i$ ,  $\rho_i$ , and  $R_i$ . The densities  $\rho_i$  and the radii  $R_i$  are constrained by observed values of  $C/mR^2$ ,  $C_m/C$ , and total mass  $m$ . These are three equations in the six unknowns  $\rho_i$  and  $R_i$ . But  $R_m = R$ , and if we specify the inner core parameters  $\rho_s$  and  $R_s$ , the three remaining variables  $\rho_f$ ,  $\rho_m$ , and  $R_f$  are determined. If we use the values of these parameters so derived along with the assumptions for  $\rho_s$  and  $R_s$  in the  $\epsilon$  and  $\xi$  equations, the latter can be solved uniquely for the  $\epsilon_i$  and  $\xi_i$ . The internal structure so obtained is consistent with the observables  $J_2 = 5.03 \times 10^{-5}$ ,  $C_{22} = 0.809 \times 10^{-5}$ ,  $C/mR^2 = 0.346$ ,  $C_m/C = 0.431$ , and  $M = 3.301 \times 10^{26} \text{g}$ . The values of  $J_2$ ,  $C_{22}$ , and  $M$  come from Smith *et al.* (2012), and  $C/mR^2$  and  $C_m/C$  from Margot *et al.* (2012). In summary there are 12 unknowns ( $3\epsilon_s, 3\xi_s, 3\rho_s, 3R_s$ ) and 10 equations ( $C/mR^2, C_m/C, m, R, J_2, C_{22}$ , two equipotential surface conditions at the CMB and two at the ICB). We can specify the inner core radius  $R_s$  and density  $\rho_s$  reducing the unknowns to 10. This exercise is carried out in Appendix A, and results are given in Table 1 for an inner core of radius  $0.6R$  and density  $8 \text{g/cm}^3$  and alternatively, for no inner core. The ICB may be more likely to be an equipotential surface than the CMB. In evaluating the consequences of the pressure torque on the equilibrium spin axis positions for an axially symmetric CMB with no solid inner core, we consider both the equipotential value of  $\epsilon_f = 7.161 \times 10^{-5}$  given in Table 1 and double this value, where the latter is a crude measure of the effects of the CMB not being an equipotential surface. Also shown in Table 1 are the measured surface ellipticities and the rotational ellipticity of the CMB. Because of Mercury's slow rotation, the centrifugal potential (Eq. (50)) has a negligible effect on the overall values of  $\epsilon_i$  and is neglected in the solution for the ellipticities. Similarly, the averaged solar potential (Eq. (51)), comparable in magnitude to the centrifugal potential, is also neglected. The large discrepancies between the observed surface ellipticities and those consistent with  $J_2$  and  $C_{22}$  might be removed by accounting for the distribution of lower-density crustal material.

The torque on the mantle due to the fluid pressure  $P$  at the CMB is

$$\mathbf{T}_p = \iint_S \mathbf{r} \times \mathbf{n} P dS = \iiint_V \mathbf{r} \times \nabla P dV, \quad (24)$$

where  $\mathbf{r}$  is the vector from the center of Mercury to a point on the CMB, and  $\mathbf{n}$  is the normal to the CMB directed outward at that point. The surface integral is over the CMB, and the volume integral, which follows from the divergence theorem, is over the fluid core. The pressure torque is zero for a spherically symmetric CMB, but a hydrostatic CMB is distorted by the asymmetric

Table 1: Interior densities, outer core radii, and ellipticities for two choices of solid inner core properties. The measured ellipticities from MESSENGER spacecraft data are provided by M. E. Perry and R.J. Phillips (private communication, 2013), and the rotational ellipticity is that of the rotational equipotential surface at the CMB.

Densities						
$R_s/R$	$\rho_s \text{ g/cm}^3$	$\rho_f \text{ g/cm}^3$	$\rho_m \text{ g/cm}^3$	$R_f \text{ km}$		
0.6	8.0	6.510	3.347	2027		
0.0	-	7.254	3.203	1998		

Ellipticities						
$R_s/R$	$\epsilon_s$	$\epsilon_f$	$\epsilon_m$	$\zeta_s$	$\zeta_f$	$\zeta_m$
0.6	$6.818 \times 10^{-5}$	$6.952 \times 10^{-5}$	$1.755 \times 10^{-4}$	$4.214 \times 10^{-5}$	$3.396 \times 10^{-5}$	$1.170 \times 10^{-4}$
0.0	-	$7.161 \times 10^{-5}$	$1.797 \times 10^{-4}$	-	$4.607 \times 10^{-5}$	$1.156 \times 10^{-4}$
Measured		-	$\sim 6.86 \times 10^{-4}$	-	-	$\sim 5.07 \times 10^{-4}$
Rotation		$3.79 \times 10^{-7}$	-	-	-	-

gravitational field and only slightly by the centrifugal and solar potentials.

For simplicity we evaluate the pressure torque under the assumption that Mercury’s CMB is axially symmetric. This assumption allows procedures in the literature for the Earth’s core–mantle boundary to be used (e.g., Melchior, 1986), and we will see that the pressure torque is so dominant that refinements from axial asymmetry cannot change the overall results but seriously complicate the analysis. The usefulness of the volume integral expression for the pressure torque comes from the relations

$$\begin{aligned} \nabla P &= -\rho_f \nabla \Phi - \rho_f \frac{d\mathbf{v}}{dt}, \\ \frac{d\mathbf{v}}{dt} &= \frac{\partial \mathbf{v}}{\partial t} + (\mathbf{v} \cdot \nabla) \mathbf{v}, \end{aligned} \quad (25)$$

where  $\Phi$  is the gravitational potential and  $\mathbf{v}$  is the velocity of the core fluid, which satisfies  $\mathbf{v} \cdot \mathbf{n} = 0$ . The first equation is a form of Newton’s second law in which pressure and gravity forces are expressed per unit volume ( $-\nabla P - \rho_f \nabla \Phi$ ). The second equation invokes the material derivative and accounts for advection. We assume steady precession in the orbit frame so that  $\partial \mathbf{v} / \partial t = 0$ . (Note that Eqs. (25) are written under the assumption that the  $x'y'z'$  system is inertial, when in fact the orbit frame is precessing. However, since the time scale for the orbital precession is so much longer than that of the spin precession within the orbit system, the deviations from  $\partial \mathbf{v} / \partial t$  in the orbit frame from 0 are negligibly small.) The potential term in Eq.(25) consists of the external potential due to the Sun and the internal potentials from the distorted layers. However, the latter can exert a gravitational torque only if the layers are misaligned. We ignore the pressure torques from the internal potentials. The pressure torque from the external potential is evaluated in Appendix B, where it is shown to add to the gravitational torque on the mantle as if a thin layer of density  $\rho_f$  that lies outside the largest sphere that fits inside the

CMB were included with the mantle in calculating the gravitational torque on the latter. That fluid layer is precisely the core contribution to  $J_2$  and  $C_{22}$ , so if there is no inner core or it is otherwise neglected, the torque on the mantle due to the Sun is for the full values of  $J_2$  and  $C_{22}$  to account for that contribution to the pressure torque. Only the  $(\mathbf{v} \cdot \nabla)\mathbf{v}$  term in  $\nabla P$  remains to be determined.

We modify the procedure outlined by Melchior (1986) and approximate the CMB surface given by Eq. (23) with  $\xi = 0$  as the ellipsoid with semiaxes  $a > c$ .

$$x'^2 + y'^2 + \frac{a^2}{c^2} z'^2 = x'^2 + y'^2 + f_\epsilon z'^2 = a^2, \quad (26)$$

where  $x', y', z'$  are non-rotating coordinates,  $x'y'$  is the equator plane of Mercury, and  $f_\epsilon = 1 + 2\epsilon$  to first order in  $\epsilon$ , where  $\epsilon = (a - c)/r_0$  is the ellipticity that appears in Eq. (23). The primes on  $x', y', z'$  distinguish these coordinates from the rotating coordinates  $x, y, z$ . (Note that this equation could not be written in the non rotating frame for an axially asymmetric CMB, which is the motivation for choosing the axially symmetric case.) The normal to this surface is given by

$$\mathbf{n}' = \frac{\nabla a^2}{|\nabla a^2|} = \frac{x'\mathbf{i}' + y'\mathbf{j}' + f_\epsilon z'\mathbf{k}'}{\sqrt{x'^2 + y'^2 + f_\epsilon^2 z'^2}} \quad (27)$$

We can transform the ellipsoid to a homologous Poincaré sphere with  $x'' = x', y'' = y', z'' = f_\epsilon z'$ , where  $\mathbf{n}'' = (x''\mathbf{i}'' + y''\mathbf{j}'' + z''\mathbf{k}'')/r_0$  is the normal to the sphere. Consistent with the Poincaré (1910) result that the fluid core has a uniform vorticity (rigid body rotation), the fluid velocity in the sphere is

$$\mathbf{v}'' = \dot{\psi}_f \times \mathbf{r} = (\dot{\psi}_{fy'z''} - \dot{\psi}_{fz'y''})\mathbf{i}' + (\dot{\psi}_{fz'x''} - \dot{\psi}_{fx'z''})\mathbf{j}' + (\dot{\psi}_{fx'y''} - \dot{\psi}_{fy'x''})\mathbf{k}', \quad (28)$$

which becomes, after converting back to the ellipsoid,

$$\mathbf{v} = (\dot{\psi}_{fy'z'} - \dot{\psi}_{fz'y'})\mathbf{i}' + (\dot{\psi}_{fz'x'} - \dot{\psi}_{fx'z'})\mathbf{j}' + \frac{(\dot{\psi}_{fx'y'} - \dot{\psi}_{fy'x'})}{f_\epsilon}\mathbf{k}', \quad (29)$$

which is the velocity in the ellipsoid. Note that the condition  $\mathbf{v} \cdot \mathbf{n}' = 0$  is satisfied and that  $\nabla \cdot \mathbf{v} = 0$ .

$$(\mathbf{v} \cdot \nabla)\mathbf{v} = (v_{z'}\dot{\psi}_{fy'} - v_{y'}\dot{\psi}_{fz'})\mathbf{i}' + (v_{x'}\dot{\psi}_{fz'} - v_{z'}\dot{\psi}_{fx'})\mathbf{j}' + \frac{(v_{y'}\dot{\psi}_{fx'} - v_{x'}\dot{\psi}_{fy'})}{f_\epsilon}\mathbf{k}'. \quad (30)$$

With the  $\nabla\Phi$  contribution to  $\nabla P$  accounted for earlier, we can write  $\nabla P = -\rho_f(\mathbf{v} \cdot \nabla)\mathbf{v}$  and integrate each component of the gradient as a guide to  $P(x', y', z')$ . The function

$$P = -\rho_f \left[ \frac{x'y'\dot{\psi}_{fy'}\dot{\psi}_{fx'}}{f_\epsilon} + z'x'\dot{\psi}_{fz'}\dot{\psi}_{fx'} + z'y'\dot{\psi}_{fz'}\dot{\psi}_{fy'} - (x'^2 + z'^2)\frac{\dot{\psi}_{fy'}^2}{2f_\epsilon} - (x'^2 + y'^2)\frac{\dot{\psi}_{fz'}^2}{2} - (y'^2 + z'^2)\frac{\dot{\psi}_{fx'}^2}{2f_\epsilon} \right] \quad (31)$$

produces the components of  $\nabla P$  except for  $f_\epsilon$  missing in the denominator of two terms in the  $\mathbf{k}$  component of the gradient. To first order in  $\epsilon$  with  $r_0 \rightarrow R_f$ ,

$$\mathbf{r} \times \mathbf{n}' = \frac{f_\epsilon - 1}{R_f}(y'z'\mathbf{i}' - x'z'\mathbf{j}') \quad (32)$$

contains the factor  $\epsilon$ , so  $f_\epsilon$  in the denominator becomes 1 in the integrand of Eq. (24) to first order in  $\epsilon$ . Integration of Eq. (24) after substitution of Eqs.(31) and (32) yields

$$\mathbf{T}_p = -\frac{8\pi}{15}\rho_f\epsilon_f R_f^5 \dot{\psi}_{fz'}(\dot{\psi}_{fy'}\mathbf{i}' - \dot{\psi}_{fx'}\mathbf{j}'), \quad (33)$$

where the contribution to  $\mathbf{T}_p$  from the external potential is not included here, but the contribution by the latter follows from the assumption that the gravitational torque on the mantle plus crust e corresponds to the full values of  $J_2$  and  $C_{22}$  (Appendix B).

The pressure torque on the core is the negative of that on the mantle. The potential part of the pressure torque on the mantle is equivalent to the gravitational torque on the thin layer of core fluid outside the largest sphere that fits inside the CMB. The negative of this torque, part of the pressure torque on the core, exactly cancels the direct gravitational torque on the core, and we need not include either this part of the pressure torque on the core or the direct gravitational torque on the core in the coupled equations. The negative of Eq. (33) is thereby the only torque on the core. Eq. (33) must be written in terms of the variables of Eq. (3). Recall that  $\mathbf{i}'$  and  $\mathbf{j}'$  are unit vectors in Mercury's equator plane that do not rotate with the planet. The term in the parentheses in Eq. (33) is  $-\mathbf{k}' \times \dot{\psi}_f$ , so the choice of the  $x'y'$  axes is arbitrary. We choose the  $x'$  axis to lie along the node of the equator on the orbit plane, such that

$$\begin{aligned} \mathbf{i}' &= \frac{q_m}{\sqrt{q_m^2 + p_m^2}}\mathbf{I} + \frac{p_m}{\sqrt{p_m^2 + q_m^2}}\mathbf{J} \\ \mathbf{j}' &= -\frac{p_m\sqrt{1-p_m^2-q_m^2}}{\sqrt{p_m^2+q_m^2}}\mathbf{I} + \frac{q_m\sqrt{1-q_m^2-p_m^2}}{\sqrt{p_m^2+q_m^2}}\mathbf{J} + \sqrt{p_m^2+q_m^2}\mathbf{K}, \end{aligned} \quad (34)$$

where definitions of  $p_m$  and  $q_m$  in terms of  $i_m$  and  $\Omega_m$  are used. With  $\mathbf{k}' = p_m\mathbf{I} - q_m\mathbf{J} + \sqrt{1-p_m^2-q_m^2}\mathbf{K}$  and a similar expression for  $\mathbf{k}'_f$  and with  $\dot{\psi}_{fz'} = \dot{\psi}_f\mathbf{k}'_f \cdot \mathbf{k}'$ ,  $\dot{\psi}_{fx'} = \dot{\psi}_f\mathbf{k}'_f \cdot \mathbf{i}'$ , and  $\dot{\psi}_{fy'} = \dot{\psi}_f\mathbf{k}'_f \cdot \mathbf{j}'$ , we can write

$$\begin{aligned} \dot{\psi}_{fx'} &= \dot{\psi}_f \left( \frac{p_f q_m}{\sqrt{p_m^2 + q_m^2}} - \frac{q_f p_m}{\sqrt{p_m^2 + q_m^2}} \right) \\ \dot{\psi}_{fy'} &= \dot{\psi}_f \left( -\frac{p_f p_m \sqrt{1-p_m^2-q_m^2}}{\sqrt{p_m^2+q_m^2}} - \frac{q_f q_m \sqrt{1-p_m^2-q_m^2}}{\sqrt{p_m^2+q_m^2}} + \sqrt{(1-p_f^2-q_f^2)(p_m^2+q_m^2)} \right) \\ \dot{\psi}_{fz'} &= \dot{\psi}_f \left[ p_f p_m + q_f q_m + \sqrt{(1-p_f^2+q_f^2)(1-p_m^2-q_m^2)} \right]. \end{aligned} \quad (35)$$

Substitution of Eqs. (35) and (34) into Eq. (33) yields  $\mathbf{T}_p$  in terms of the variables of Eq. (3).

This completes the development of the appropriate torques acting on Mercury's mantle and core. These torques are substituted into the components of  $\mathbf{N}_m$  and  $\mathbf{N}_f$  in Eqs.(3).

### 3. Results

We apply the dissipative torques separately to determine the effect of each for a spherically symmetric CMB. In each case, the final state is determined by running the calculations until free

librations in longitude are completely damped, and there is no longer any change in a very small circulation of the spin vector around the mean position of the equilibrium state. We calculate the evolution for the tides alone for a solid planet whose moment of inertia  $C/mR^2 = 0.346$  (Margot et al. 2012). We are interested in the final evolutionary state of Mercury’s spin, so we start the system close to that state. Fig. 2 shows an example of the damping of the free librations in longitude for tidal evolution alone with  $k_2/Q = 0.004$  (Van Hoolst and Jacobs (2003) calculate values of  $k_2 \sim 0.37$  to  $0.6$  for a range of core sulfur content and inner core radii. The value of  $k_2/Q$  chosen is for a typical  $Q$  value near 100.) The second panel in Fig. 2 shows the damping of the precessional amplitude with viscous and pressure torques applied. The general behavior of the system for any of the individual core–mantle torques is similar to that displayed in Fig. 2, although the final equilibrium positions as well as the time scales to reach equilibrium differ. For example, for the tides alone the time scale to reach equilibrium exceeds 20 million years, whereas that for the viscous torque with the parameters for the right panel of Fig. 2 is on the order of a million years.

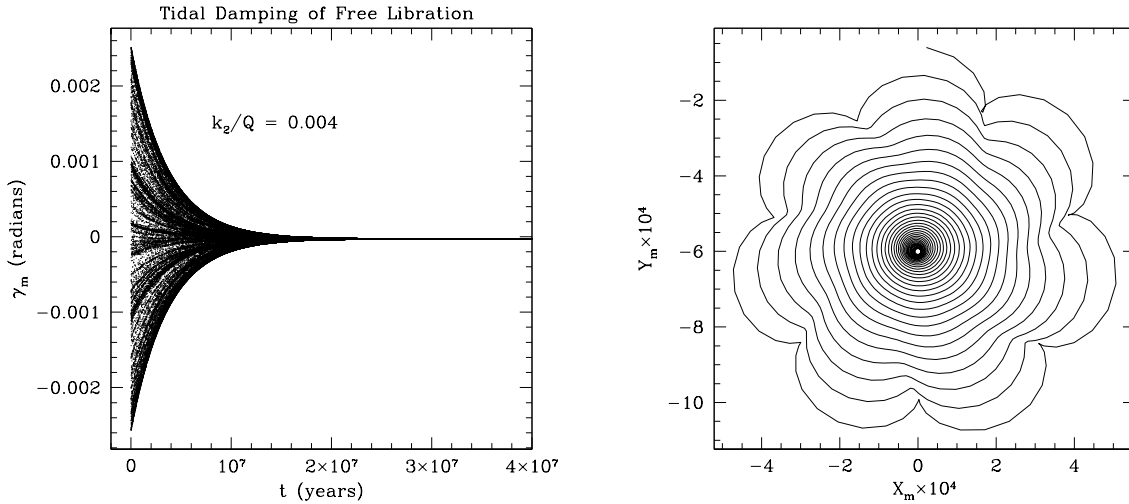


Fig. 2.— Example of damping the initial free libration for tidal torques alone (left panel) and the precession amplitude of the mantle for pressure torque and viscous torque (right panel), where  $k_2/Q = 0.004$  for the left panel and viscosity  $\nu = 2.25 \times 10^5 (1.0) \text{ cm}^2/\text{s}$  for the right panel.  $X_m$  and  $Y_m$  indicate the position of the unit vector along the mantle spin axis projected onto the  $XY$  orbit plane. Since the angles are small, the coordinates represent radians ( $6 \times 10^{-4} \text{ rad} = 2.06 \text{ arcmin}$ ). Initial conditions:  $(i_m, \Omega_m) = (0.1^\circ, 0^\circ)$ ,  $(i_f, \Omega_f) = (0.1^\circ, 180^\circ)$ ,  $\gamma_m = 0.1^\circ$ ,  $\dot{\gamma}_m = 0.0001^\circ/\text{day}$ , and  $\dot{\gamma}_f = 0.0001^\circ/\text{day}$ .

### 3.1. Tidal evolution

Tidal evolution for a solid Mercury essentially takes the system to the Cassini state, as shown in the left panel of Fig. 3. The Cassini state is in fact defined for the solid planet with the full moment of inertia. The final equilibrium states for viscous core–mantle coupling are also shown in Fig. 3 for several values of the kinematic viscosity  $\nu$ . The small circles in this figure traced by the projection of the spin onto the XY plane are the endpoints of the evolution; the small circles result from the precession of the perihelion of Mercury’s orbit. The projection of the spin axis onto the orbit plane makes one revolution around a small circle as the perihelion argument  $\omega$  makes one half revolution. The radii of the circles are less than the maximal 1 arcsec fluctuations in the position of spin relative to the instantaneous Cassini state because of variations in the solar system parameters that determine the state (Peale, 2006). Peale (1974) showed that the definition of the Cassini state as being coplanar with the orbit and Laplace plane normals is a good approximation, where the argument of perihelion is absorbed into the libration angle. The small scatter of the equilibrium positions of the spin for different values of  $\omega$  shown in Fig. 3 displays the deviations from the approximate solution defining the state; these deviations are considerably smaller than the one standard deviation ( $1\sigma \sim 5$  arcsec) observational uncertainty in the position of the spin axis indicated by the small ellipse (Margot *et al.*, 2012).

When any of the dissipative CMB torques is turned on, it completely dominates the tidal torque on the mantle, except in the limit of very small coupling. In this limit, both the tidal torque and the small CMB torque drive the mantle spin to another Cassini state appropriate to the moment of inertia of the mantle alone ( $C_m/mR^2 = 0.149$ ) at a smaller obliquity. For stronger core–mantle coupling, the final equilibrium states of the mantle spin for all the CMB torques are not distinguishably altered by the tidal torques.

### 3.2. Viscous coupling

The final equilibrium states of the system for viscous coupling between the core and mantle displayed in Table 2 and Fig. 3 show large offsets of the spin axis from the Cassini state. Each viscosity in a pair for the two relaxation time scales yields the same value of  $\beta$  (Eqs. (12) and (13)). The relatively short time scale for approaching the equilibrium state indicated in the right panel of Fig. 2 is typical of the viscous coupling as well as the magnetic and topographic coupling considered below. The offset is largest for the smallest viscosities, and one must increase the core–mantle coupling to bring the spin axis to within the uncertainty of the observed position. The kinematic viscosity  $\nu \sim 15 \text{ cm}^2/\text{s}$  or  $\nu \sim 8.75 \times 10^5 \text{ cm}^2/\text{s}$  for the two relaxation time scales for this condition to be satisfied. Binding the core more strongly to the mantle means that Mercury approaches the motion of a solid planet, and hence the mantle will end up closer to the Cassini state so defined.

The large differential rotation between the mantle and core induced by the orbit precession is initially surprising. The mantle spin is projected onto the fourth quadrant of the XY orbit

Table 2: Equilibrium positions (projections) ( $X_i, Y_i$ ) and phase of mantle ( $\gamma_m$ ) and deviation of core angular velocity from  $1.5n$  ( $\dot{\gamma}_f/n$ ) for viscous coupling (Fig. 3). The equilibrium angular velocity of the mantle is  $\equiv 1.5n$ . The last line shows the equilibrium position for tidal evolution of a completely solid Mercury.

$\nu \text{ cm}^2/\text{s}$	$X_m \times 10^4$	$Y_m \times 10^4$	$X_f \times 10^2$	$Y_f \times 10^2$	$\gamma_m \times 10^4$	$\dot{\gamma}_f/n \times 10^3$
0.001, $7.15 \times 10^3$	0.4050	-2.6176	1.7282	0.1466	-0.2979	-14.6552
0.01, $2.26 \times 10^4$	1.1600	-3.0221	5.1764	12.9136	-0.5569	-12.9136
0.1, $7.15 \times 10^4$	1.6421	-4.6545	7.3584	5.7722	-0.6586	-6.5967
1.0, $2.26 \times 10^5$	0.8275	-5.7003	3.5782	0.8374	-0.4675	-0.8374
15.0, $8.75 \times 10^5$	0.2576	-5.9385	0.9787	0.0037	-0.3346	-0.0373
Tide	0.0	-5.9256			-2.8457	

plane, whereas the core spin is projected onto the first quadrant, which is shown schematically in Fig. 4. The direction of the viscous torque is proportional to  $\dot{\psi}_m - \dot{\psi}_f$ . That this torque is perpendicular to the precessional angular velocity can be inferred from the figure. An evaluation of all the torques on the core and mantle when the system has reached the equilibrium position confirms the simultaneous precession of both with the precession of the orbit, as they must to be stationary in the orbit frame of reference. What has happened is that the core and mantle have assumed positions such that the total torque on each is just that necessary to cause each to precess with the orbit. When the coupling is weak, the vector separation of the spins of mantle and core is increased to provide the necessary torques, which in turn leaves the mantle more separated from the Cassini state. The equilibrium values of the parameters for viscous coupling are shown in Table 2 for  $\omega = 0$ . Notice that the core rotation about the spin axis is slightly below the spin-orbit resonant value of  $1.5n$ . The mantle always ends up with  $\dot{\gamma}_m \equiv 0$ , and the latter is omitted from Table 2.

The kinematic viscosity of the Earth’s core has a wide range of estimates. From damping of nutational motions, Smylie *et al.* (2009) determined a value near the CMB close to  $\nu \sim 2900 \text{ cm}^2/\text{s}$ . But from laboratory measurements and theoretical simulations that limit the variation of viscosity of liquid iron with pressure,  $\nu \sim 10^{-2} \text{ cm}^2/\text{s}$  (de Wijs *et al.* 1998). Vočadlo (2007) discussed the 14 orders of magnitude range in the estimates of Earth’s core viscosity, but she favored the laboratory and theoretical estimates that place the value of  $\nu$  near that of water at Earth’s surface. All of the group of small viscosities in Fig. 3 fall within the smaller range spanned by the two estimates by de Wijs *et al.* (1998), but the group of large viscosities all exceed the larger value. If Mercury has a solid layer of FeS at the base of the mantle that separated from an Fe–S–Si mixture in the core (Hauck *et al.*, 2013), the fluid adjacent to the CMB might be a slurry of solid FeS particles with a viscosity comparable to or even exceeding the larger viscosities in Fig. 3. There remains almost an unconstrained uncertainty in the core viscosity.

Since the differential rotation of the core and mantle is relatively large (up to several degrees separating the spin vectors), it is prudent to check the energy dissipation resulting from the differential motion. The rate of work being done by the viscous core–mantle torque on the core

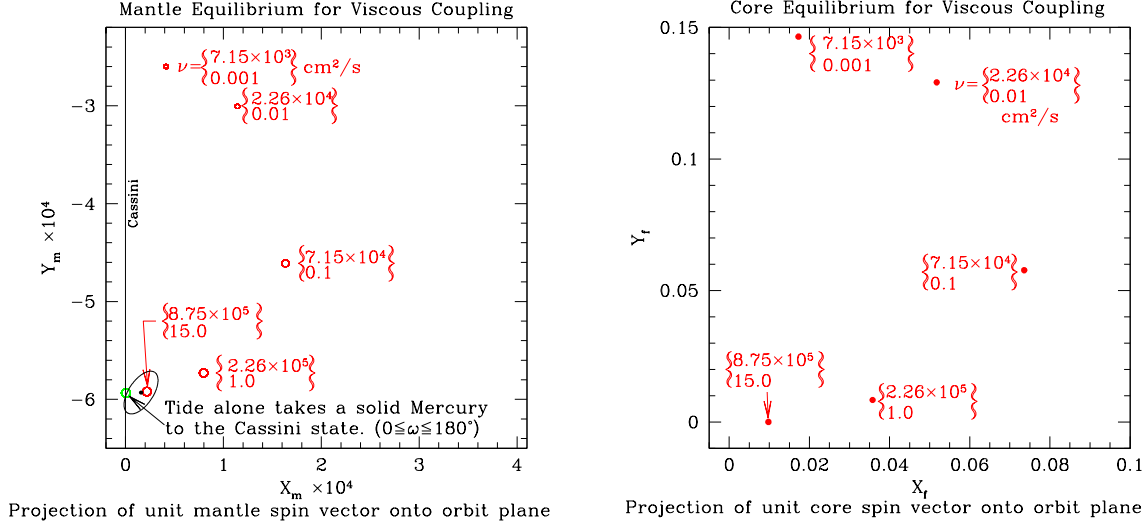


Fig. 3.— Equilibrium offset of the mantle spin axis from the Cassini state and corresponding positions of the core spin axis for two types of viscous coupling and several values of the viscosity (Table 2). The pairs of viscosities at each point refer to the same value of the coupling constant  $\beta$  for viscosity time scales  $R_f/(\nu\dot{\psi})^{1/2}$  (smaller viscosity) and  $R_f^2/\nu$  (larger viscosity) discussed in the text. A viscosity  $\sim 8.75 \times 10^5$  (or 15)  $\text{cm}^2/\text{s}$  is necessary to bring the spin axis to within the  $1\sigma$  uncertainty (small ellipse) in the pole position near the Cassini state for the two time scales. In the left panel the small circles describe the variation of the final equilibrium position as the perihelion longitude varies. The equilibrium state of the mantle for tidal evolution of a completely solid Mercury is also shown by the small circle on the line labeled Cassini, which is the intersection of the plane containing the Cassini state (spin vector), the orbit normal (at  $X_m, Y_m = 0, 0$ ), and the Laplace plane normal (at  $X_m, Y_m = 0, 0.15$ ) with the orbit plane. The best observational determination of the spin position is the dot in the center of the  $1\sigma$  uncertainty ellipse.

is just the scalar product of this torque and the differential angular velocity. Hence,

$$\frac{dW}{dt} = \beta(\dot{\psi}_m - \dot{\psi}_f) \cdot (\dot{\psi}_m - \dot{\psi}_f). \quad (36)$$

The components of  $\dot{\psi}_m$  and  $\dot{\psi}_f$  are given in Table 2; the scalar magnitudes are  $\dot{\psi}_m = 1.5n$  and  $\dot{\psi}_f = (1.5n + \dot{\gamma}_f)$ . From Eqs. (12) and (13) we find  $\beta = 9.307 \times 10^{29}$  and  $3.605 \times 10^{31} \text{ g cm}^2/\text{s}$ , respectively, for  $\nu = 2.26 \times 10^4, 0.01$  and  $8.75 \times 10^5, 15 \text{ cm}^2/\text{s}$ . Also,  $(\dot{\psi}_m - \dot{\psi}_f)^2 = 3.809 \times 10^{-2} n^2$  and  $2.188 \times 10^{-4} n^2$  for the two extremes, respectively. Then

$$\begin{aligned} \frac{dW}{dt} &= 2.423 \times 10^{16} \text{ erg/s}, \quad \nu = (2.26 \times 10^4, 0.01) \text{ cm}^2/\text{s}, \\ &= 1.213 \times 10^{16}, \text{ erg/s} \quad \nu = (8.75 \times 10^5, 15.0) \text{ cm}^2/\text{s}. \end{aligned} \quad (37)$$

The rate at which the torque does work is smaller in spite of the larger viscosity because the relative motion of the core and mantle is so much smaller that it overcompensates the larger viscosity.

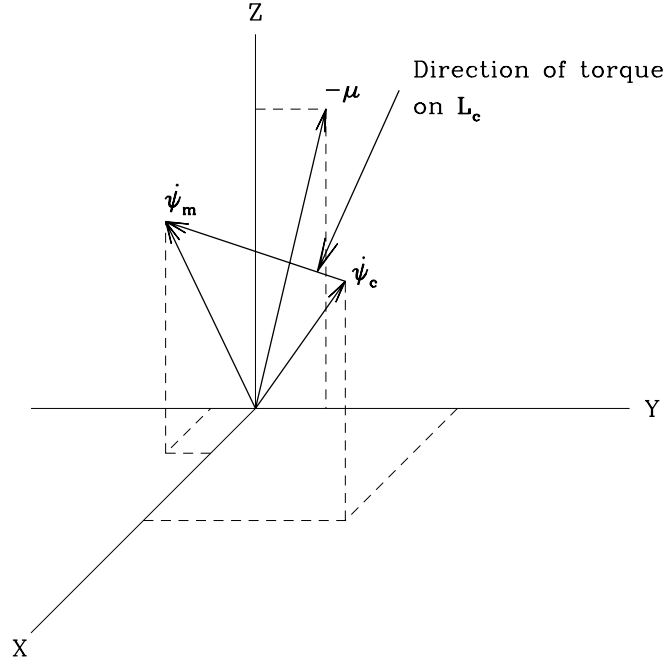


Fig. 4.— Schematic of the final positions of the unit spin vectors of the core and mantle for one of the smaller viscosities in Fig 3. The torque on the core causes the precise precession of the core with the orbit.

The consequence of the torque on the core is to make the core precess with the orbit (core spin fixed in the orbit frame). The work done on the core by the torque is an upper bound on the energy dissipated. To judge the importance of this dissipation, we compare it with the radioactive heat production in the mantle and with the rate at which energy is conducted into the mantle at the CMB.

The current radioactive heat production in the Earth’s mantle is  $\sim 7.4 \times 10^{-8}$  erg/(gs) from  $^{238}\text{U}$ ,  $^{235}\text{U}$ ,  $^{232}\text{Th}$ , and  $^{40}\text{K}$  (Turcotte and Schubert, 2002). Peplowski *et al.* (2011) find that the current radioactive heat generation from K, Th, and U on Mercury’s surface is near  $2 \times 10^{-7}$  erg/(gs). Michel *et al* (2013) and Tosi *et al.* (2013) model Mercury’s thermal history constrained by present day surface heat production, global contraction estimates, and time frames of magma production. Both models are consistent with about a factor of three enhancement in the concentration of radioactive elements on the surface compared with the current mantle concentration, which leads to a current mantle heat production near  $7 \times 10^{-8}$  erg/(gs)—comparable to that in the Earth’s mantle. For a core radius of 2000 km, a mean Mercury radius of 2440 km, and a mean mantle density near  $3.2 \text{ g/cm}^3$  (Table 1), the total radioactive heat production in the mantle is near  $6.5 \times 10^{18}$  erg/s with no contribution from the crust.

Alternatively, for the conduction of heat into the mantle at the CMB, the thermal conductivity of FeS is  $K_1 = 3.5 \times 10^5$  erg/(s cm K) at 308 K (Table 3 of Clauser and Huenges, 1995). There

are few data on the temperature and pressure dependence of thermal conductivity of FeS, but that for single crystal FeS<sub>2</sub> varies inversely with temperature between 200 and 300 K (Popov *et al.*, 2013). If we assume a similar dependence for FeS, the thermal conductivity  $K_1$  could be as small as  $7 \times 10^4$  erg/(s cm K) at 1500 K. This low value could be compensated somewhat by an increase in the conductivity due to pressure (*e.g.*, Clauser and Huenges, 1995) at the depth of the FeS layer, so we choose  $K_1 = 1 \times 10^5$  erg/(s cm K) for the FeS layer. The thermal conductivity of basalt is near  $K_2 = 2 \times 10^5$  erg/(s cm K) for a wide range of temperature and pressure (Figs. 2 and 3 in Clauser and Huenges, 1995).

With  $R_f$ ,  $R_{FeS}$ , and  $R$  the radii of the core, FeS layer, and the planet, we can write for a steady state flux of heat  $F$

$$\begin{aligned} -\frac{dT}{dr} &= \frac{F}{4\pi K_1 r^2} & R_f < r < R_{FeS} \\ -\frac{dT}{dr} &= \frac{F}{4\pi K_2 r^2} & R_{FeS} < r < R. \end{aligned} \quad (38)$$

Integration of these equations over the range of radii where each is applicable yields two equations that give the difference in temperatures  $T_R$  and  $T_{FeS}$  between  $R$  and  $R_{FeS}$  and separately  $T_{FeS}$  and  $T_{R_f}$  between  $R_{FeS}$  and  $R_f$ . Eliminating  $T_{FeS}$  from these equations, we can solve for the flux  $F$  in terms of  $T_{R_f} - T_R$ ,  $K_1$ ,  $K_2$ ,  $R$ ,  $R_{FeS}$ , and  $R_f$ . With  $F = -4\pi R_f^2 K_1 dT/dr$  at  $R_f$ , we can solve for the temperature gradient at the CMB appropriate to the conductivities and a given temperature difference between a layer close to the surface and the CMB.

$$\left. \frac{dT}{dr} \right|_{R_f} = \frac{T_{R_f} - T_R}{R_f \left[ \frac{R_f}{R_{FeS}} - 1 + \frac{K_1}{K_2} \left( \frac{R_f}{R} - \frac{R_f}{R_{FeS}} \right) \right]}. \quad (39)$$

Solutions of the interior structure show that it is statistically unlikely for the thickness of a solid FeS layer at the base of the mantle to exceed 90 km (Hauck *et al.*, 2013). With  $R_f = 2040$  km,  $R_{FeS} = 2130$  km,  $R = 2440$  km,  $T_{R_f} = 1500$  K (near the melting point of FeS),  $T_R = 300$  K (as an average temperature over a surface a short distance below the surface of Mercury), and the above values of the conductivity coefficients, we find  $dT/dr|_{R_f} = 5.706 \times 10^{-5}$  K/cm.

Substitution of this gradient back into the expression for  $F$  yields

$$F = 2.98 \times 10^{18} \text{ erg/s}. \quad (40)$$

The maximum viscous dissipation at the CMB of  $2.423 \times 10^{16}$  or  $1.213 \times 10^{16}$  erg/s for the extremes in the viscosity pairs is less than a 1% contribution to either the radioactive heat production in the mantle or the heat flux from normal thermal conduction at the CMB, and should thus not alter the temperature distribution or any observable quantity significantly. Below we show that pressure coupling restricts the differential rotation between core and mantle to much smaller values, so viscous dissipation will contribute even less to the total heat flux.

### 3.3. Magnetic coupling

Magnetic dipole coupling leads to behavior similar to that of the viscous coupling with the offset of the mantle spin axis from the Cassini state being quite large for the observed value of the magnetic moment of  $2.43 \times 10^{19} \text{Am}^2$  (Fig. 5). The equilibrium positions of the mantle spin progress in an arc toward the Cassini state as the coupling is increased by increasing the magnetic dipole moment. This coupling is for a centered dipole, whereas Mercury’s dipole is offset to the north by about 486 km (Anderson *et al.*, 2011, 2012). However, since the coupling is so small, it was thought unnecessary to recover no more than a factor of a few in the coupling magnitude with the offset dipole. Instead, we determine the equilibrium positions of the spin axes for a root mean square (rms) value of the radial component of the field  $B_r$  on the CMB. A value of the magnetic dipole moment necessary to bring the spin axis close to the Cassini state is a factor of 100 more than the value inferred from the external field measurements. The rms value of  $B_r$  is  $2.5 \times 10^{-5} \text{T}$  for the same condition. For comparison, the rms value of  $B_r$  is  $2.25 \times 10^{-7} \text{T}$  on the CMB for the observed dipole field. The parameter values at the equilibrium state for magnetic coupling are given in Table 3 for  $\omega = 0$ . Magnetic coupling between the core and mantle is clearly not sufficient to bring the spin axis of the mantle to within the observational uncertainty of its position for magnetic field strengths at the CMB inferred from measurements in the magnetosphere.

Table 3: Equilibrium positions (projections)  $(X_i, Y_i)$  and phase of the mantle ( $\gamma_m$ ) and the deviation of core angular velocity from  $1.5n$  ( $\dot{\gamma}_f/n$ ) for magnetic coupling (Fig. 5). The upper half of the table is for dipole coupling only with the first column being the factor multiplying the measured magnetic moment for Mercury of  $2.83 \times 10^{19} \text{Am}^2$ . The lower half of the table gives equilibrium positions for rms values of  $B_r$  on the CMB from all harmonic components of the field.

Moment	$X_m \times 10^4$	$Y_m \times 10^4$	$X_f \times 10^2$	$Y_f \times 10^2$	$\gamma_m \times 10^4$	$\dot{\gamma}_f/n \times 10^3$
1.0	0.0961	-2.7593	0.0065	14.9464	-0.0119	-41.7039
10×	1.0735	-3.1859	5.0955	12.9856	-0.2487	-43.1722
15×	1.5921	-4.1803	7.4812	8.4525	-0.3688	-28.4403
20×	1.4759	-5.1006	6.8718	4.3378	-0.3419	-14.8230
30×	0.8639	-5.8424	3.9929	1.0750	-2.0014	-3.8547
100×	0.0843	-6.1011	0.3885	0.0511	-0.0192	-0.0384
$\sqrt{\langle B_r^2 \rangle}$	$X_m \times 10^4$	$Y_m \times 10^4$	$X_f \times 10^2$	$Y_f \times 10^2$	$\gamma_m \times 10^4$	$\dot{\gamma}_f/n \times 10^3$
$5 \times 10^{-6} \text{T}$	1.3538	-3.4892	6.2491	11.6587	-0.3232	-13.2290
$7 \times 10^{-6} \text{T}$	1.6396	-4.4886	7.5437	7.1573	-0.3771	-8.1619
$1 \times 10^{-5} \text{T}$	1.2703	-5.4904	5.8239	2.6697	-0.2921	-3.0930
$2.5 \times 10^{-5} \text{T}$	0.2474	-6.0838	1.1325	0.02394	-0.0569	-0.0963
$5 \times 10^{-5} \text{T}$	0.0634	-6.1016	0.2846	-0.0557	-0.0143	-0.00605

Some insight into what is happening for equilibrium, when the spin axes of both the core and mantle are stationary in the precessing orbit frame, can be found by examining the magnetic dipole coupling positions in Fig. 5. For the observed magnetic dipole moment, the spin

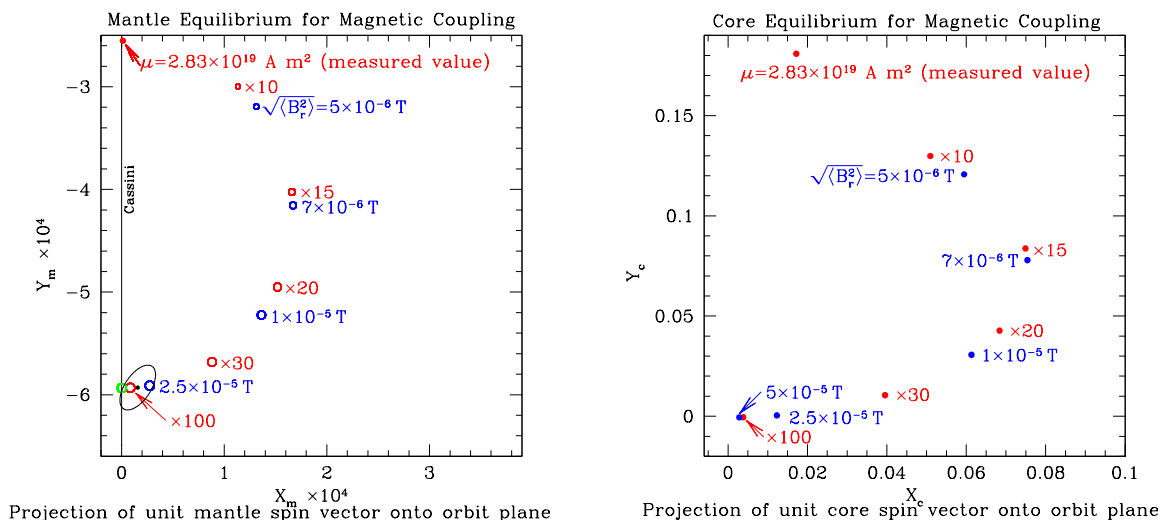


Fig. 5.— Equilibrium offset of the mantle spin axis from the Cassini state and corresponding positions of the core spin axis for magnetic core–mantle coupling for several values of the magnetic dipole moment  $\mu$  and separately for an rms value of  $B_r$  on the CMB for dipole plus higher-order terms (Table 3). For dipole coupling alone, a magnetic moment that is 100 times the value of  $2.38 \times 10^{19} \text{ A m}^2$  inferred from the magnetic field measurements is necessary to bring the spin of the mantle to within the uncertainty in the pole position. Alternatively, an rms value of  $B_r \gtrsim 2.5 \times 10^{-5} \text{ T}$  is required. Other details in this figure are as in Fig. 3.

axis is nearly in the plane defined by the Laplace plane normal and the orbit plane normal. This is again a Cassini state, but for a planetary moment of inertia corresponding to that of the mantle alone ( $0.149mR^2$  instead of  $0.346mR^2$ ). In other words, the coupling is so weak that the mantle rotates as if the core were not there. The similar behavior for the other core–mantle coupling torques as the strength of the coupling is varied means they would all approach this other Cassini state in the limit of weak coupling.

### 3.4. Topographic coupling

The distribution of equilibrium positions for the mantle and core for topographic coupling is shown in Fig. 6. The behavior is again similar to the other two core–mantle coupling processes. Since the ad hoc efficiency  $\zeta \leq 1$  and  $\sin \delta \leq 1$ , the product cannot be sufficiently large to bring the spin axis close to the observed value. So the modeled topography apparently cannot provide sufficient coupling between core and mantle to this end. Table 4 shows the parameter values appropriate to topographic core–mantle coupling.

Like magnetic coupling, topographic coupling between mantle and core also fails to bring the spin axis to within the observational uncertainty of its position. Only viscous coupling re-

Table 4: Equilibrium positions (projections) ( $X_i, Y_i$ ) and phase of the mantle ( $\gamma_m$ ) and deviation of the core angular velocity from  $1.5n$  ( $\dot{\gamma}_f/n$ ) for topographic coupling (Fig. 6).

$\zeta \sin \delta$	$X_m \times 10^4$	$Y_m \times 10^4$	$X_f \times 10^2$	$Y_f \times 10^2$	$\gamma_m \times 10^4$	$\dot{\gamma}_f/n \times 10^3$
0.00001	0.0	-2.5465	0.0200	14.9830	-0.0239	-0.1315
0.0001	0.1155	-2.5520	0.5034	14.9268	-0.0259	-0.1322
0.001	0.8627	-2.7890	3.8690	13.8924	-0.1979	-0.1097
0.01	1.6937	-4.2230	7.6860	7.3440	-0.3845	-0.0391
0.1	1.3000	-5.3174	5.8260	2.7530	-0.2992	-0.0083
1.0	0.8266	-5.7599	3.4400	0.6980	-0.1659	-0.0017

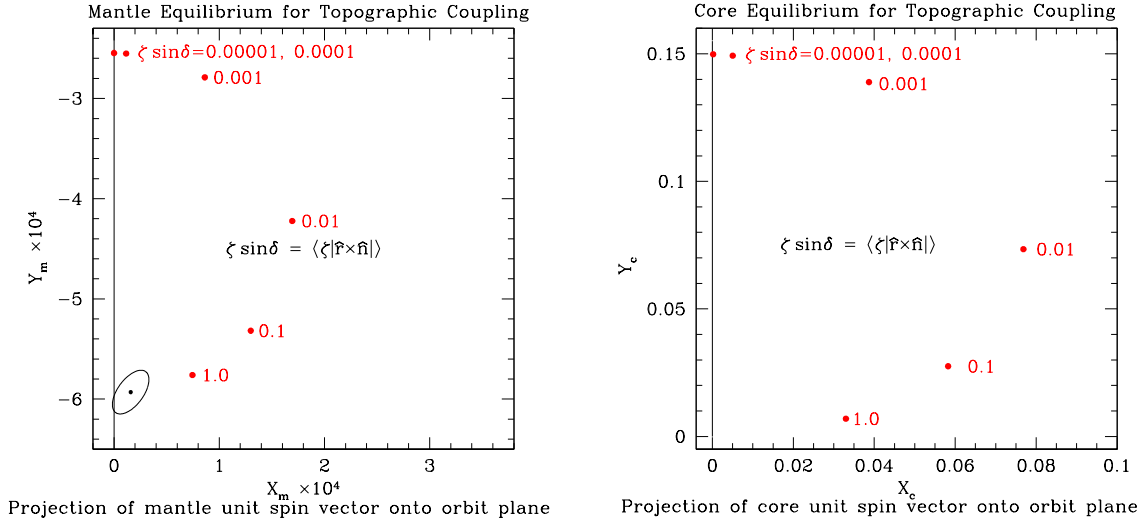


Fig. 6.— Equilibrium offset of the mantle spin axis from the Cassini state and corresponding positions of the core spin axis for topographic core–mantle coupling for several values of slopes of CMB bumps (Table 4). Even the maximum value of  $\zeta \sin \delta = 1.0$  is insufficient to bring the mantle spin to within the uncertainty ellipse locating the mantle spin position.

mains as a possibility. Even the latter is possible only for relatively large values of the viscosity that may not prevail.

### 3.5. Pressure coupling

The ellipsoidal shape of the CMB leads to pressure torques between core and mantle that result in far different behavior from that of the dissipative torques alone. With the pressure torque in effect, viscous dissipation now brings the mantle spin to the Cassini state for any value of the viscosity and for either of the values of  $\epsilon_f = 7.161 \times 10^{-5}$  (hydrostatic) or  $1.432 \times 10^{-4}$  (non hydrostatic) for an axisymmetric CMB (Fig. 7). The equilibrium positions of the core spin for the two values of  $\epsilon_f$  are much closer to the mantle spin position than they were for the dissipative

processes alone, and they lie nearly in the plane containing the Cassini state displaced away from the Laplace plane normal.

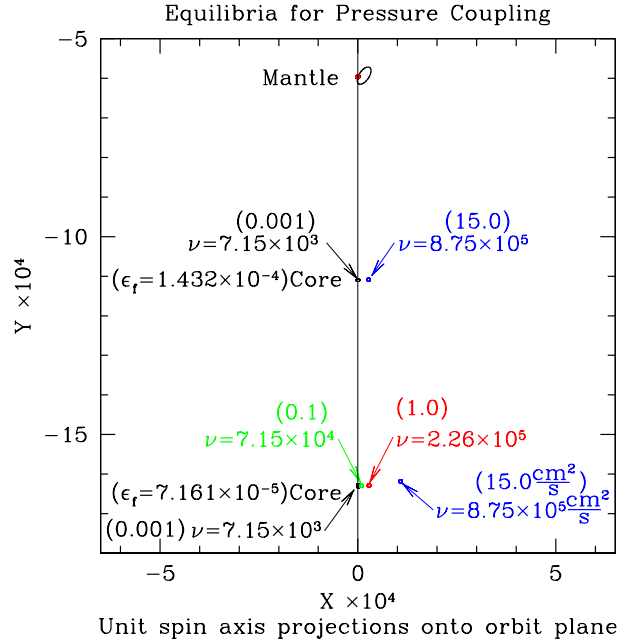


Fig. 7.— Equilibrium positions of mantle and core spins for pressure and viscous coupling at the CMB.  $\nu$  values are for the viscous time scales; parentheses denote  $\nu$  values for Greenspan and Howard time scales. The values of  $\epsilon_f$  appropriate for the two groups of core positions are indicated in parentheses.

We have included viscous dissipation as the most likely process that can influence the spin positions of the core and mantle with pressure coupling, although tidal, magnetic, or topographic dissipation will also work on longer time scales. In all cases shown in Fig. 7 the mantle spin separation from the Cassini state is immeasurably small. The largest displacement of the mantle spin axis toward the fourth quadrant is 0.055 arcsec for  $\epsilon_f = 7.161 \times 10^{-5}$  and  $\nu = 8.75 \times 10^5$  or  $15 \text{ cm}^2/\text{s}$ . This value is reduced to 0.016 arcsec for the larger  $\epsilon_f = 1.432 \times 10^{-4}$ . The observational uncertainty ellipse for the mantle spin is included in the figure. The core spin has joined the mantle spin by being nearly on the Cassini state line and separated from the mantle spin by 3.55 arcmin for the smaller hydrostatic  $\epsilon_f$  and by 1.77 arcmin for the larger  $\epsilon_f$  in the direction away from the Laplace plane normal. Increasing the CMB ellipticity forces the core spin to be closer to that of the mantle. As the viscosity is increased, the core spin lags the retrograde precession of the Cassini plane by greater amounts, with the displacement near 23 arcsec for the hydrostatic  $\epsilon_f$  and kinematic viscosity  $\nu = 8.75 \times 10^5$  or  $15 \text{ cm}^2/\text{s}$  but lagging only 5.6 arcsec for the  $\epsilon_f$  that is double the hydrostatic value.

The core spin displacement is consistent with the classical solution of Poincaré (1910) for Earth’s core, for which the consequence for the core flow of the mantle precession is a uniform vorticity (consistent with our assumption of the core rotating uniformly) with the vorticity vec-

tor displaced from the symmetry (rotation) axis of the CMB by a small angle in the direction away from the negative of the precession vector. Our displacements of core spin from mantle spin of 3.55 and 1.77 arcmin are much larger than the  $O(1)$  arcsec displacement that Melchior (1986) found for Earth’s core. But Earth is spinning more rapidly, and the precession rates are far different. The lag of the core spin behind the precessing Cassini plane is consistent with the results of Stewartson and Roberts (1963), Roberts and Stewartson (1965), and Busse (1968), who found a lag for the spin of the Earth’s core in the same direction for the effect of viscous dissipation. Here our final state for Mercury is obtained by dissipative evolution starting from an arbitrary initial state.

#### 4. Summary and conclusions

We have calculated the evolution of Mercury’s mantle spin axis under conservative and dissipative torques. Tidal torque alone brings a solid Mercury to Cassini state 1 with only a negligibly small offset of the mantle spin axis from the Cassini state. But each of the three dissipative core–mantle interactions, treated alone, can lead to equilibrium positions of the spin axis that are far outside the uncertainties in its observed position. For viscous coupling, a kinematic viscosity  $\nu \sim 8.75 \times 10^5$  or  $15\text{cm}^2/\text{s}$  is needed to bring the spin axis within the  $1\sigma$  uncertainty in the observed position. For magnetic dipole coupling, the magnetic moment must be 100 times larger than that observed by the MESSENGER spacecraft to satisfy the same constraint. The rms value of the radial component of the magnetic field  $\sqrt{B_r^2}$  on the CMB that can include the offset dipole field and all the multipole fields is  $2.5 \times 10^{-5}\text{T}$ , which is two orders of magnitude greater than the rms value of the dipole field at the CMB and one order of magnitude greater than the estimated rms radial field from MESSENGER observations (C. L. Johnson, personal communication, 2012). The observed magnetic field does not provide sufficient coupling between the core and mantle to be consistent with the observed position of the pole. Finally there appears to be no physically possible slope of the topography on the CMB that can bring the mantle spin axis to within the uncertainty in its observed position.

The core maintains a differential rotation for all the dissipative equilibrium positions, and the difference increases as the coupling decreases. As the core–mantle coupling is increased to the point where the mantle spin axis equilibrium approaches the Cassini state, the core spin approaches the orbit normal. This state can be only temporary if the coupling continues to increase, as eventually the core would be rigidly attached to the mantle, the spins would be parallel and would occupy the Cassini state for a completely solid Mercury, and the mantle would no longer librate independently of the core.

The ellipsoidal CMB leads to pressure coupling between the core and mantle that completely controls the final equilibrium positions of the spins, although the dissipative coupling is still necessary to effect the evolution. The pressure torque in the presence of viscous (or any other) dissipation drives the mantle spin to the Cassini state with negligible dissipative displacement. The final position of the core spin is displaced by a few arcmin from the mantle

spin approximately in the Cassini plane in a direction away from the negative of the precession vector. The viscous dissipation causes the core spin to lag the precession of the Cassini plane by an amount that increases with the viscosity (23 arcsec for the largest viscosities shown in Fig 7), a configuration that is consistent with similar results for the Earth’s core. Unfortunately the close occupancy of the Cassini state forced by the pressure coupling precludes using an offset of the mantle spin to constrain the dissipative properties of Mercury’s interior, and there is no obvious way to determine the core spin orientation. At the same time, we are assured of the theoretical occupation of the Cassini state by Mercury’s spin, which is so far consistent with the observed position. This means that the constraints on the interior structure that depend on knowledge of the Cassini state obliquity are secure (*e.g.* Hauck, *et al.* 2013).

An unlikely caveat to this conclusion is the influence of a non-spherical solid inner core. This influence is suppressed by the pressure force on the inner core such that the effective density of a deformed inner core is  $\rho_s - \rho_f$  for its gravitational interaction with the Sun and with the mantle. If the light element depressing the melting temperature of the fluid core is silicon instead of sulfur, the density differential between the fluid and the solid inner core is small (Hauck et al., 2013). Still, it is of interest to determine the behavior of the inner core for the sulfur impurity and its possible influence on the equilibrium positions of the observable mantle spin vector. Our conjecture is that this latter influence is negligibly small, which is supported by the observed position of the spin axis being consistent with occupancy of the Cassini state, but this conjecture should be verified. Since some of the assumptions incorporated in this work, such as the uniform vorticity of the fluid core found by Poincaré, may not be appropriate as the thickness of the fluid core is reduced, we choose to investigate the solid inner core behavior in a future work.

## 5. Acknowledgments

We thank Tim Van Hoolst and Marie Yseboodt and an unknown referee for careful reviews with suggestions that greatly improved and clarified the manuscript. SJP is grateful for the support of this work provided by the Planetary Geology and Geophysics Program of NASA under grant NNX08AI76G. Without the superlative performance of the engineers and managers of The Johns Hopkins University Applied Physics Laboratory (APL) during the MESSENGER mission, the values of  $J_2$ ,  $C_{22}$ ,  $C/mR^2$ ,  $C_m/C$ , and  $M$  used to constrain interior models of Mercury could not have been obtained. The MESSENGER project is supported by the NASA Discovery Program under contracts NASW-00002 to the Carnegie Institution of Washington and NAS-97271 to APL.

## Appendix A: Interior surface shapes

We consider a model with three homogeneous layers, mantle–crust, fluid outer core, and solid inner core. Using the generic expression for the moment of inertia of a uniform sphere,

$2mR^2/5 = 8\pi\rho R^5/15$  ( $R = \text{radius}$ ,  $m = \text{mass}$ ,  $\rho = \text{density}$ ), we can write expressions for  $C/mR^2$  and  $C_m/C$  ( $C$  is principal moment of inertia about spin axis, and  $C_m$  is that of the mantle plus crust) derived from observables in terms of  $R$ ,  $R_f$ ,  $R_s$ ,  $\rho_m$ ,  $\rho_f$ , and  $\rho_s$ , where the subscripts  $m$ ,  $f$ , and  $s$  refer to mantle, fluid outer core, and solid inner core, respectively. A third equation results from the total mass in terms of the same variables. With  $R_f/R \rightarrow R_f$ ,  $R_s/R \rightarrow R_s$ ,  $\rho_m/\bar{\rho} \rightarrow \rho_m$ ,  $\rho_f/\bar{\rho} \rightarrow \rho_f$ , and  $\rho_s/\bar{\rho} \rightarrow \rho_s$  as normalized variables, where  $\bar{\rho} = \text{the mean density of Mercury}$ ,

$$\begin{aligned} R_s^3\rho_s + (R_f^3 - R_s^3)\rho_f + (1 - R_f^3)\rho_m &= 1 \\ \frac{2}{5} \left[ R_s^5\rho_s + (R_f^5 - R_s^5)\rho_f + (1 - R_f^5)\rho_m \right] &= \frac{C}{mR^2} \\ \left[ R_s^5\rho_s + (R_f^5 - R_s^5)\rho_f + (1 - R_f^5)\rho_m \right] \frac{C_m}{C} &= (1 - R_f^5)\rho_m \end{aligned} \quad (41)$$

Eqs. (41) are three equations in the five unknowns  $\rho_m$ ,  $\rho_f$ ,  $\rho_s$ ,  $R_f$ , and  $R_s$ . If we specify  $R_s$  and  $\rho_s$ , the radius and density of the solid inner core, the equations can be solved for the remaining unknowns.

To determine the gravitational distortion of the CMB and the inner core radius, we need expressions for the harmonic coefficients  $J_2$  and  $C_{22}$  in terms of the ellipticities of the surfaces. For uniform ellipsoids with axes  $a > b > c$ , the principal moments of inertia  $A < B < C$  are given by  $A = M(b^2 + c^2)/5$ ,  $B = M(a^2 + c^2)/5$ ,  $C = M(a^2 + b^2)/5$  with  $M = 4\pi abc\rho/3$ . Then  $B - A = M(a^2 - b^2)/5 = M(a - b)(a + b)a/5a \approx 8\pi\rho\xi r_0^5/15$  to first order in the equatorial ellipticity  $\xi = (a - b)/r_0$ , where  $r_0$  is the mean radius of the ellipsoid. Similarly  $C - A = 8\pi\rho\epsilon_a r_0^5/15$  and  $C - B = 8\pi\rho\epsilon_b r_0^5/15$  to first order in the polar ellipticities  $\epsilon_a = (a - c)/r_0$  and  $\epsilon_b = (b - c)/r_0$ . For a three-layer model with each layer homogeneous,

$$\begin{aligned} C_{22} &= \frac{B - A}{4mR^2} = \sum_{i=1}^3 \frac{\rho_i}{10} (\xi_i R_i^5 - \xi_{i-1} R_{i-1}^5) \\ &= \frac{1}{10} \left[ \rho_m \xi_m + (\rho_f - \rho_m) \xi_f R_f^5 + (\rho_s - \rho_f) \xi_s R_s^5 \right] \end{aligned} \quad (42)$$

$$\begin{aligned} J_2 &= \frac{1}{mR^2} \left( \frac{C - A}{2} + \frac{C - B}{2} \right) = \sum_{i=1}^3 \frac{2\rho_i}{5} (\epsilon_i R_i^5 - \epsilon_{i-1} R_{i-1}^5) \\ &= \frac{2}{5} \left[ \rho_m \epsilon_m + (\rho_f - \rho_m) \epsilon_f R_f^5 + (\rho_s - \rho_f) \epsilon_s R_s^5 \right], \end{aligned} \quad (43)$$

where  $\epsilon = (\epsilon_a + \epsilon_b)/2$  is a mean polar ellipticity and the variables are normalized as in Eqs. (41). If we choose  $\rho_s$  and  $R_s$ , and use Eqs. (41) to determine  $\rho_m$ ,  $\rho_f$ , and  $R_f$  from the observables  $M$ ,  $C/mR^2$ , and  $C_m/C$ , the additional observables  $J_2$  and  $C_{22}$  in Eqs. (42) and (43) give us two equations with the  $\xi$  and  $\epsilon$  values as unknowns. To obtain additional equations in these unknowns we assume that Mercury is hydrostatic so that boundaries between layers of different densities are equipotential surfaces, which we now determine.

For our homogeneous layers we assume a surface of the following form.

$$r = r_0 \left[ 1 - \frac{2\epsilon}{3} P_{20}(\cos \theta) + \frac{\xi}{6} P_{22}(\cos \theta) \cos 2\phi \right], \quad (44)$$

where  $r_0$  is a mean radius, and  $P_{20}$  and  $P_{22}$  are Legendre functions. This expression leads to a surface mass distribution

$$\sigma(\theta, \phi) = \sigma_0 - \frac{2}{3} \epsilon r_0 \rho P_{20}(\cos \theta) + \frac{1}{6} \xi r_0 \rho P_{22}(\cos \theta) \cos 2\phi, \quad (45)$$

where  $\sigma_0$ , a mean surface mass density, is typically set to zero. The potential at a point  $r(\theta, \phi) > r_0$  of a surface mass element  $dm = \sigma(\theta, \phi)dA$ , where  $dA = r'^2 \sin \theta' d\theta' d\phi'$  is the element of surface area, is

$$\begin{aligned} dV &= -\frac{Gdm}{|\mathbf{r} - \mathbf{r}'|} = -\frac{G\sigma(\theta', \phi')dA}{(r'^2 + r^2 - 2rr' \cos S)^{1/2}} \\ &= -\frac{G\sigma(\theta', \phi')dA}{r} \sum_{l=0}^{\infty} \left(\frac{r'}{r}\right)^l P_l(\cos S) \\ &= -\frac{G\sigma(\theta', \phi')r'^2 \sin \theta' d\theta' d\phi'}{r} \\ &\quad \times \sum_{l=0}^{\infty} \sum_{m=0}^l (2 - \delta_{0m}) \frac{(l-m)!}{(l+m)!} \left(\frac{r'}{r}\right)^l P_{lm}(\cos \theta) P_{lm}(\cos \theta') \cos m(\phi - \phi'), \end{aligned} \quad (46)$$

where  $S$  is the angle between  $\mathbf{r}'$  and  $\mathbf{r}$  and where the primed coordinates refer to the source point  $dm$  ( $r' = r'(\theta', \phi')$ ), and the unprimed coordinates ( $r = r(\theta, \phi)$ ) to the field point where the potential is evaluated. In Eq. (46)  $P_l$  are Legendre polynomials,  $P_{lm}$  are Legendre functions, and  $\delta_{0m}$  is the Kronecker delta. Substitution of Eq.(45) into the last of Eqs. (46) and integration over the surface yields terms only for  $(l, m) = (0, 0)$ ,  $(2, 0)$ , and  $(2, 2)$  because of the orthogonality of the Legendre functions. Replacing  $r'$  by  $r_0$ , we find the potential external to the given surface distribution of mass,

$$V_{ext} = -\frac{4\pi G\sigma_0 r'^2}{r} + \frac{8\pi G\rho r_0^5 \epsilon}{15 r^3} \left( \frac{3}{2} \cos^2 \theta - \frac{1}{2} \right) - \frac{6\pi G\rho r_0^5 \xi}{15 r^3} \sin^2 \theta \cos 2\phi. \quad (47)$$

If  $r < r_0$ , the expansion is

$$dV = \frac{-G\sigma(\theta', \phi')dA}{r_0} \sum_{l=0}^{\infty} \left(\frac{r}{r_0}\right)^l P_l(\cos S). \quad (48)$$

In Eq. (48),  $r^2/r_0^3$  replaces  $r_0^2/r^3$  in  $V_{ext}$  for the  $l = 2$  terms. For the  $l = 0$  term,  $r_0$  in the denominator and numerator cancels, so the potential interior to the surface distribution of mass becomes

$$V_{int} = -4\pi G\sigma_0 r_0 + \frac{8\pi}{15} Gr^2 \rho \epsilon \left( \frac{3}{2} \cos^2 \theta - \frac{1}{2} \right) - \frac{6\pi}{15} Gr^2 \rho \xi \sin^2 \theta \cos 2\phi. \quad (49)$$

The centrifugal potential is given by

$$V_{rot} = \frac{\dot{\psi}^2 r^2}{3} [P_{20}(\cos \theta) - 1], \quad (50)$$

where  $\dot{\psi} = 3n/2$  is the rotation rate. The lowest-order external potential due to the Sun is averaged around the orbit to remove the variable part as Mercury rotates and changes its distance.

$$\langle V_{\odot} \rangle = -n^2 \left[ -\frac{1}{2} \frac{r^2}{(1-e^2)^{3/2}} P_{20}(\cos \theta) + r^2 \left( \frac{7e}{2} - \frac{123e^3}{16} + \dots \right) P_{22}(\cos \theta) \cos 2\phi \right]. \quad (51)$$

Comparison of Eqs. (50) and (51) shows that they are comparable in magnitude. We indicate below that the centrifugal potential causes a change in the ellipticities of the boundaries of the surfaces only in the third significant figure, so both the centrifugal and the averaged solar potential will be omitted when calculating the ellipticities although they are displayed in the equations.

In the following we can ignore central and constant terms. The potential at the CMB is the sum of internal and external potentials of the various layers, all evaluated at  $r = R_f$ . We can consider the  $P_{20}$  and  $P_{22}$  terms separately. Positive contributions to the magnitude of the CMB potential from the  $P_{22}$  terms come from the internal potential for the outer surface with density  $\rho_m$  and ellipticity  $\xi_m$ , from the internal potential at the CMB with density  $\rho_f$  and ellipticity  $\xi_f$ , and from the external potential from the inner core boundary (ICB) with density  $\rho_s$  and ellipticity  $\xi_s$ . Negative contributions at the CMB come from material removed from the mantle (from the protrusion of the ellipsoidal outer core) with density  $\rho_m$  and ellipticity  $\xi_f$  and from material removed from the fluid outer core at the ICB with density  $\rho_f$  and ellipticity  $\xi_s$ . If this is to be an equipotential surface it must equal  $-gh$  where  $g$  is the local acceleration of gravity and  $h$  is given by the  $P_{22}$  term in Eq. (44). Then

$$\left\{ -\frac{n^2 R_f^2}{4} \left( \frac{7e}{2} - \dots \right) + \frac{2\pi G}{15} \left[ \rho_m \xi_m R_f^2 + (\rho_f - \rho_m) \xi_f R_f^2 + (\rho_s - \rho_f) \xi_s \frac{R_s^5}{R_f^3} \right] \right\} P_{22}(\cos \theta) \cos 2\phi = \frac{4\pi G}{3} \left[ \rho_f R_f + (\rho_s - \rho_f) \frac{R_s^3}{R_f^2} \right] \frac{\xi_f R_f}{6} P_{22}(\cos \theta) \cos 2\phi,$$

where we have added the averaged potential due to the Sun. The bracketed term on the right side of the above equation is the acceleration of gravity at the CMB, and the variables are now dimensioned. With cancellations

$$-\frac{n^2 R_f^2}{4} \left( \frac{7e}{2} - \dots \right) + \rho_m \xi_m R_f^2 + (\rho_f - \rho_m) \xi_f R_f^2 + (\rho_s - \rho_f) \xi_s \frac{R_s^5}{R_f^3} = \frac{5}{3} \left[ \rho_f R_f^2 + (\rho_s - \rho_f) \frac{R_s^3}{R_f} \right] \xi_f \quad (52)$$

A similar procedure leads to an expression for the  $\epsilon_s$  from the equipotential surface at the CMB, where  $h$  is now the  $P_{20}$  term in Eq. (44), and where we have added the non-radial part of the centrifugal potential and the averaged potential from the Sun.

$$\frac{\dot{\psi}_m^2 R_f^2}{3} + \frac{n^2 r^2}{2(1-e^2)^{3/2}} + \rho_m \epsilon_m R_f^2 + (\rho_f - \rho_m) \epsilon_f R_f^2 + (\rho_s - \rho_f) \epsilon_s \frac{R_s^2}{R_f^3} = \frac{5}{3} \left[ \rho_f R_f^2 + (\rho_s - \rho_f) \frac{R_s^3}{R_f} \right] \epsilon_f \quad (53)$$

For the ICB only inner potentials are involved, all evaluated at  $r = R_s$ . Again setting the potential at the ICB equal to the local  $-gh$ , we find for the  $\xi$ s and  $\epsilon$ s

$$-\frac{n^2 R_s^2}{4} \left( \frac{7e}{2} + \dots \right) + \rho_m \xi_m + (\rho_f - \rho_m) \xi_f + (\rho_s - \rho_f) \xi_s = \frac{5}{3} \rho_s \xi_s \quad (54)$$

$$\frac{\dot{\psi}_s^2 R_s^2}{3} + \rho_m \epsilon_m + (\rho_f - \rho_m) \epsilon_f + (\rho_s - \rho_f) \epsilon_s = \frac{5}{3} \rho_s \epsilon_s. \quad (55)$$

Eqs. (42), (52), and (54) are three equations in the three unknowns  $\xi_i$ , and Eqs. (43), (53), and (55) are three equations in the three unknowns  $\epsilon_i$ . Table 1 in the main text gives the solutions for  $\rho_s = 8 \text{ g/cm}^3$ ,  $R_s = 0.6R$  and for  $R_s = 0$  (no solid inner core). Because of Mercury's slow rotation, the centrifugal contribution to the potentials makes a change only in the third significant decimal place in the solutions for the  $\epsilon_i$ , so it and the comparable contribution from the averaged solar potential are neglected in these solutions.

### Appendix B: Potential contribution to pressure torque

The contribution to the pressure torque from the external potential  $\Phi$  in Eqs. (24) and (25) is

$$\mathbf{\Gamma}_{P\odot} = - \iint_S \mathbf{r}' \times \mathbf{n} \rho_f \Phi dS, \quad (56)$$

where  $\mathbf{r}'(\theta', \phi')$  is a radius vector to a point on the CMB measured from the center of Mercury,  $\mathbf{n}$  is the surface normal and

$$\Phi = -\frac{Gm_\odot}{r} \sum_{l=0}^{\infty} \sum_{m=0}^l \left( \frac{r'}{r} \right)^l (2 - \delta_{0m}) \frac{(l-m)!}{(l+m)!} P_{lm}(\cos \theta) P_{lm}(\cos \theta') \cos m(\phi - \phi'), \quad (57)$$

is the potential of the Sun interior to Mercury, with  $r, \theta, \phi$  the spherical coordinates of the Sun in Mercury's principal axis system. With the surface of the CMB represented by  $r' = R_f(1 - (2\epsilon_f/3)P_{20}(\cos \theta') + (\xi_f/6)P_{22}(\cos \theta') \cos 2\phi')$  (Eq.(44)), we can form the function

$$H = r' - R_f[1 - (2\epsilon_f/3)P_{20}(\cos \theta') + (\xi_f/6)P_{22}(\cos \theta') \cos 2\phi'], \quad (58)$$

so that

$$\mathbf{n} = \frac{\nabla H}{|\nabla H|} = \hat{\mathbf{e}}_r - \cos \theta' \sin \theta' (2\epsilon_f + \xi_f \cos 2\phi) \hat{\mathbf{e}}_{\theta'} + \xi_f \sin \theta' \sin 2\phi' \hat{\mathbf{e}}_{\phi'}, \quad (59)$$

where  $R_f/r' = 1$  to first order in  $\epsilon$  or  $\xi$  ( $|\nabla H|$  is  $O(1 + \epsilon^2 \text{ or } \xi^2)$ ) and

$$\mathbf{r}' \times \mathbf{n} = -R_f[\cos \theta' \sin \theta' (2\epsilon_f + \xi_f \cos 2\phi) \hat{\mathbf{e}}_{\phi'} + \xi_f \sin \theta' \sin 2\phi' \hat{\mathbf{e}}_{\theta'}]. \quad (60)$$

Substitution of Eqs. (60) and (57) into Eq. (56) yields the pressure torque on the CMB from the solar potential. For the integration over the surface, we convert the unit vectors in spherical coordinates to unit vectors in Cartesian coordinates with  $\hat{\mathbf{e}}_{\phi'} = -\sin \phi' \mathbf{i} + \cos \phi' \mathbf{j}$  and  $\hat{\mathbf{e}}_{\theta'} = \cos \theta' \cos \phi' \mathbf{i} + \cos \theta' \sin \phi' \mathbf{j} - \sin \theta' \mathbf{k}$ . All the terms in the  $\mathbf{i}$  and  $\mathbf{j}$  components of the integrand contain the product  $\cos \theta' \sin \theta'$ , which select only the  $P_{21}(\cos \theta') = -3 \sin \theta' \cos \theta'$  term in  $\Phi$ ,

and the  $\mathbf{k}$  component contains  $\sin^2 \theta'$ , which selects only the  $P_{22}(\cos \theta')$  term in  $\Phi$  from the orthogonality of the Legendre functions. Integration yields

$$\begin{aligned} \Gamma_{P_\odot} = & \frac{4\pi G m_\odot}{15} \frac{R^5}{r^3} \rho_f [(-2\epsilon_f + \xi_f) P_{21}(\cos \theta) \sin \phi \mathbf{i} \\ & + (2\epsilon_f + \xi_f) P_{21}(\cos \theta) \cos \phi \mathbf{j} + \xi_f P_{22}(\cos \theta) \sin 2\phi \mathbf{k}]. \end{aligned} \quad (61)$$

Recall from Appendix A that  $B' - A' = 8\pi\rho\xi R^5/15$ , to first order in  $\xi$ , is the moment of inertia difference of a thin layer of material outside the largest sphere that would fit inside the ellipsoid. Similarly  $C' - A'$  and  $C' - B'$  are the same expressions with  $\xi$  replaced by  $\epsilon_a$  and  $\epsilon_b$ , respectively, and  $\epsilon = (\epsilon_a + \epsilon_b)/2$ . Then we can rewrite the components of Eq. (61) as

$$\begin{aligned} (\Gamma_{P_\odot})_x &= \frac{G m m_\odot R^2}{r^5} (\mathbf{r} \cdot \mathbf{k})(\mathbf{r} \cdot \mathbf{j})(3J'_2 - 6C'_{22}), \\ (\Gamma_{P_\odot})_y &= -\frac{G m m_\odot R^2}{r^5} (\mathbf{r} \cdot \mathbf{k})(\mathbf{r} \cdot \mathbf{i})(3J'_2 + 6C'_{22}), \\ (\Gamma_{P_\odot})_z &= 12 \frac{G m m_\odot R^2}{r^5} (\mathbf{r} \cdot \mathbf{i})(\mathbf{r} \cdot \mathbf{j})C'_{22}, \end{aligned} \quad (62)$$

where  $J'_2 = [(C' - A')/2 + (C' - B')/2]/mR^2$  and  $C'_{22} = (B' - A')/4mR^2$ . The right sides of these equations are identical to those of Eq. (5) with  $J_2$  and  $C_{22}$  replaced by  $J'_2$  and  $C'_{22}$ . The pressure torque due to the solar potential simply adds to the gravitational torque on the mantle as if the thin layer of fluid of density  $\rho_f$  were added to the mantle. These additions are the contributions of the core to  $J_2$  and  $C_{22}$ . So if the inner core contributions are small or otherwise neglected, the gravitational torque on the mantle is that appropriate to the total  $J_2$  and  $C_{22}$  and not just the values appropriate to the mantle–crust alone.

## References

- Anderson, B.J., Johnson, C.L., Korth, H., Purucker, M.E., Winslow, R.M., Slavin, J.A., Solomon, S.C., McNutt, R.L.Jr., Raines, J.M., Zurbuchen, T.H., 2011. The global magnetic field of Mercury from MESSENGER orbital observation. *Science* 333, 1859–1862.
- Anderson, B.J., Johnson, C.L., Korth, H., Winslow, R.M., Borovsky, J.E., Purucker, M.E., Slavin, J.A., Solomon, S.C., Zuber, M.T., McNutt, R.L.Jr., 2012. Low-degree structure in Mercury’s magnetic field. *J. Geophys. Res.* 117, E00L12, doi: 10.129/2012JE001459.
- Buffett, B.A., 1992. Constraints on magnetic energy and mantle conductivity from forced nutations of the Earth. *J. Geophys. Res.* 97, 19581–19597.
- Busse, F.H., 1968. Steady flow in a precessing spheroidal shell. *J. Fluid. Mech.* 33, 739–751.
- Castillo-Rogez, J.C., Efroimsky, M., Lainey, V., 2011. The tidal history of Iapetus: Spin dynamics in the light of a refined dissipation model. *J. Geophys. Res.* 116, E09008, doi: 10.1029/2010JE003664.
- Clauser, C., Huenges, E., 1995. Thermal conductivity of rocks and minerals, In: Ahrens, T.J. Ed., *Rock Physics and Phase Relations, A Handbook of Physical Constants*, AGU Reference Shelf 3, Washington, DC, pp. 105–126.
- Colombo, G., 1966. Cassini’s second and third laws. *Astron. J.* 71, 891–896.
- Colombo, G., Shapiro, I.I., 1966. The rotation of the planet Mercury. *Astrophys. J.* 145, 296–307.
- Correia, A.C.M., Laskar, J., 2004. Mercury’s capture into the 3/2 spin–orbit resonance as a result of its chaotic dynamics. *Nature* 429, 848–850.
- Correia, A.C.M., Laskar, J., 2009. Mercury’s capture into the 3/2 spin–orbit resonance including the effect of core–mantle interaction. *Icarus* 201, 1–11.
- de Wijs, G.A., Kresse, G., Vočadlo, L., Dobson, D., Alfè, D., Gillan, M.J., Price, G.D., 1998. The viscosity of liquid iron at the physical conditions of the Earth’s core. *Nature* 392, 805–807.
- Goldreich, P., Peale, S.J., 1966. Spin–orbit coupling in the solar system. *Astron. J.* 71, 425–438.
- Greenspan, H.P., Howard, L.N., 1963. On a time-dependent motion of a rotating fluid. *J. Fluid Mech.* 17, 385–404.
- Hauck, S.A.II, Margot, J.L., Solomon, S.C., Phillips, R.J., Johnson, C.L., Lemoine, F.G., Mazarico, E., McCoy, T.J., Padovan, S., Peale, S.J., Perry, M.A., Smith, D.E., Zuber M.T., 2013. The curious case of Mercury’s internal structure. *J. Geophys. Res. Planets* 118, 1204–1220.
- Hut, P., 1981. Tidal evolution in close binary systems. *Astron. Astrophys.* 99, 126–140.

- Margot, J.L., Peale, S.J., Jurgens, R.F., Slade, M.A., Holin, I.V., 2007. Large longitude libration of Mercury reveals a molten core. *Science* 316, 710–714.
- Margot, J.L., Peale, S.J., Solomon, S.C., Hauck, S.A.II, Ghigo, F.D., Jurgens, R.F., Yseboodt, M., Giorgini, J.D., Padovan, S., Campbell, D.B., 2012. Mercury's moment of inertia from spin and gravity data, *J. Geophys. Res.* 117, E00L09, doi: 10.1029/2012JE004161.
- Melchior, P., 1986. *The Physics of the Earth's Core*, Pergamon Press, Oxford, pp. 218–222.
- Michel, N.C., Hauck, S.A., Solomon, S.C., Phillips, R.J., Roberts, J.H., Zuber, M.G. (2013) Thermal evolution of Mercury as constrained by MESSENGER observations, *J. Geophys. Res. Planets* **118**, 1033-1044.
- Mignard, F., 1979. The evolution of the lunar orbit revisited, I. *Moon Planets* 20, 301–315.
- Mignard, F., 1980 The evolution of the lunar orbit revisited, II. *Moon Planets* 23, 185–201.
- Mignard, F., 1981. The evolution of the lunar orbit revisited, III. *Moon Planets* 24, 189–207.
- Peale, S.J., 1969. Generalized Cassini's laws. *Astron. J.* 74, 483–489.
- Peale, S.J., 1974. Possible histories of the obliquity of Mercury. *Astron. J.* 79, 722–744.
- Peale, S.J., 2005. The free precession and libration of Mercury. *Icarus* 178, 4–18.
- Peale, S.J., 2006. The proximity of Mercury's spin to Cassini state 1 from adiabatic invariance. *Icarus* 181, 338–347.
- Peale, S.J., 2007 The origin of the natural satellites. In Schubert, G., Spohn, T. (Eds.) *Planets and Moons, Treatise on Geophysics, Volume 10: Moons*, Elsevier, pp. 465–508.
- Peplowski, P.N., Evans, L.G., Hauck II, S.A., McCoy, T.J., Boynton, W.V., Gillis-Davis, J.J., Ebel, D.S., Goldsten, J.O., Hamara, D.K., Lawrence, D.J., McNutt Jr., R.L., Nittler, L.R., Solomon, S.C., Rhodes, E.A., Sprague, A.L., Starr, R.D., Stockstill-Cahill, K.R. 2011. Radioactive elements on Mercury's surface from MESSENGER: Implications for the Planet's formation and evolution. *Science* 333, 850-852.
- Pettengill, G.H., Dyce, R.B., 1965. A radar determination of the rotation of the planet Mercury. *Nature* 206, 1240.
- Poincaré, H., 1910. Sur la précession des corps déformables. *Bull. Astron.* 27, 321–367.
- Popov, P.A., Fedorov, P.P., Kuznetsov, S.V., 2013. Thermal conductivity of FeS<sub>2</sub> pyrite crystals in the temperature range 50-300 K. *Crystal. Rep.* 58, 319–321.
- Roberts, P.H., Stewartson, K., 1965. On the motion of a liquid in a spheroidal cavity of a precessing rigid body. *J. Geophys. Res.* 67, 279–288.

Smith, D.E., Zuber, M.T., Phillips, R.J., Solomon, S.C., Hauck, S.A.II., Lemoine, F.G., Mazarico, E., Neuman, G.A., Peale, S.J., Margot, J.L., Johnson, C.L., Torrence, M.H., Perry, M.E., Rowlands, D.G., Goossens, S., Head, J.W., Taylor, A.H., 2012. Gravity field and internal structure of Mercury from MESSENGER. *Science* 336, 214–217.

Smylie, D.E., Brazhkin, V., Palmer, A., 2009. Direct observations of the viscosity of Earth's outer core and extrapolation of measurements of the viscosity of liquid iron. *Physics-Uspekhi* 52, 79–92.

Stewartson, K., Roberts P.H., 1963. On the motion of a liquid in a spheroidal cavity of a precessing rigid body. *J. Fluid Mech.* 17, 1–20.

Tosi, N., Grott, M., Plesa, A-C. Breuer, D. 2013, A thermo-chemical evolution of Mercury's interior, *J. Geophys. Res. Planets*, **118**, doi:10.1002/jgre.20168.

Turcotte, D.L., Schubert, G. 2002 *Geodynamics* (2nd ed.), Cambridge U. Press, Cambridge, UK, p. 137.

Van Hoolst, T., Jacobs, C. 2003 Mercury's tides and interior structure, *J. Geophys. Res.* 108 (E11), 5121, doi:10.1029/2003JE002126.

Van Hoolst, T. A. Rivoldini, R.M. Baland, M. Yseboodt, (2012) The effect of tides and an inner core on the forced longitudinal librations of Mercury, *Earth Planet. Sci. Let.*, **333-334**, 83-90.

Vočadlo, L., 2007. Core viscosity. In: Gubbins, D., Herro-Bervera, E. (Eds.), *Encyclopedia of Geomagnetism and Paleomagnetism*, Springer, pp. 104–106.